

Politecnico di Torino

DEPARTMENT OF MECHANICAL AND AEROSPACE ENGINEERING
Master of Science in Biomedical Engineering



**Live Wire: design and validation of a capacitive
coupling Intra-Body Communication system for
visually impaired people**

Candidate:
Matteo Morrone

Supervisors:
Prof. Danilo Demarchi
Prof. Alessandro Sanginario
Prof. Paolo Motto Ros
Eng. Marco Crepaldi

ACADEMIC YEAR 2020–2021

A mia Madre e mio Padre.

Abstract

Intra-Body Communication (IBC) is a non-RF, short range communication technique which uses the human body as a transmission medium ensuring a safe data exchange system. In this thesis, a new device, *Live Wire*, is treated. It is based on the use of a transmitter (TX), directly connected to ground through a low impedance path and a wearable receiver device (RX), powered by batteries and capacitively coupled to ground, thus providing a high impedance path to ground. It supports visually impaired people as a navigation indoor and object detection system providing an alternative to other biomedical Wireless Body Area Network (WBAN) techniques. Indeed its lower power consumptions and intrinsic safety in sensitive data transmission make it more suitable for such applications. First, a state of the art overview, introducing most diffused and well-known exploited techniques in literature, is provided, followed by the phenomenon theoretical background investigation. *Live Wire*, conceived by Crepaldi et al. [5] is presented, describing the key-properties of the exploited system to introduce the device at the current state, starting from its hardware design, electrical characteristics, applicability and performed functions. Then its validation measurements results, confirming the effectiveness and reliability of the designed device. Touch detection algorithm in different conditions is tested, demonstrating its accuracy. Last, the possibility to recognize RX user touch from fortuitous one, as well as all the possible future outcomes and applications, are discussed.

Contents

List of Tables	v
List of Figures	vii
1 Introduction on Intra-Body Communication	1
2 State of the art: Intra-Body Communication and Radio Frequency	4
2.1 Radio Frequency Body Area Network	4
2.1.1 ZigBee	8
2.1.2 Beacon	10
2.2 Intra-Body Communication	11
2.2.1 Capacitive coupling	15
2.2.2 Galvanic coupling:	17
2.2.3 Waveguide methods:	22
3 IBC theoretical background	23
3.1 Dielectric properties of materials and human tissues:	23
3.2 Electromagnetic field - biological tissues interaction:	27
3.2.1 Path loss as a function of frequency:	29
3.2.2 Path loss as a function of distance:	32
4 Live Wire	34
4.1 Overview	34
4.2 Design architecture and performed functions	37
4.2.1 Transceiver design and schematic	37

4.2.2	Receiver design and schematic	53
4.2.3	Power supply and connection to the PYBD	60
5	Results and Discussion	63
5.1	Touch detection	63
5.1.1	Microwave Oven	64
5.1.2	Wardrobe	68
5.1.3	Drawers	71
5.2	Power consumptions	74
6	Conclusions and Future Outcomes	77
	Bibliography	79

List of Tables

2.1	Biological effects due to an increase of temperature.	6
3.1	Numeric values of attenuation factors for surface-wave term.	29
4.1	Key properties of STM32L486RG and STM32F722: power supply range, flash memory and SRAM memory dimension, number of I/Os, number of DACs and ADCs.	35
4.2	Saturation occurrence, changing R_s and the signal amplitude. 'O' represents missing saturation, 'X' represents the presence of saturation in open circuit condition.	42
4.3	Summary of the power ports provided by PYBD.	61
5.1	Physical characteristics of subjects involved in validation measurements.	64
5.2	Power consumptions in terms of injected current for both TX and RX considering a square wave with an amplitude of 3.3 V and an amplitude equal to zero.	75
5.3	Power consumptions in terms of injected current for both TX and RX during data exchange via Bluetooth, powering both relè. Performed tests consist in 5 second in which the receiver sends data to the transceiver, then 5 seconds of pause and finally 5 seconds in which the transceiver sends data to the receiver.	75

5.4 Power consumptions in terms of injected current for both TX and RX during data exchange via Bluetooth, without powering relè. Performed tests consist in 5 second in which the receiver sends data to the transceiver, then 5 seconds of pause and finally 5 seconds in which the transceiver sends data to the receiver. 76

List of Figures

1.1	Comparison between RF and IBC techniques.	2
2.1	Taxonomy of RF techniques used for WBANs.	5
2.2	Measured path loss as a function of the distance around the torso (NLOS) and along the torso (LOS). A lower path loss characterizes Line-of-sight communication.	7
2.3	Different Zigbee topologies: Peer-to-peer, star, cluster tree and mesh topology, each one based on the use of three ZigBee devices: a coordinator, a router and an end device.	9
2.4	Comparison between RFID, Beacon, and <i>Live Wire</i> , regarding the propagation of the signal around the TX node.	10
2.5	BodyCom system working principles.	12
2.6	Representation of the device working steps. Mobile/base unit block diagram.	13
2.7	Representation of the device working steps. Mobile unit state diagram.	14
2.8	<i>Live Wire</i> architecture: the TX attached on the table is directly linked to ground and the RX can capacitively close the circuit to ground, thanks to the high impedance path.	15
2.9	Zimmerman intra-body communication model.	16
2.10	A galvanic coupling scheme for Intra-Body Communication is represented. The human body can be considered, in first approximation, a resistor. Receiving and transmitting electrodes are attached to the receiver and transmitter units, respectively, to encode the information in an AC current signal and decode after collecting it. . . .	18

3.1	Typical permittivity ϵ and conductivity σ behavior as frequency-dependent functions. ϵ decreases with the frequency as σ increases. α , β and γ dispersion regions are highlighted.	26
3.2	Path loss as a function of frequency for a distance $r = 0.001$ m from the TX.	31
3.3	Path loss as a function of frequency for a distance $r = 2$ m from the TX.	31
3.4	Path loss as a function of distance from the TX for two different frequencies: 300 MHz and 30 MHz. It is also shown the logarithmic path loss, measured as $20\log(\text{pathloss})$	33
3.5	Surface-wave, Induction-field and quasi-static field contributions to the total electric field at the receiver node as functions of distance and distance multiplied by the wave number. The plot refers to a 50 MHz wave emitted by the transmitter.	33
4.1	Top and bottom view of the microPython board.	36
4.2	Schematic of the TX module.	38
4.3	Electric model of the open circuit at the TX stage, parasitically coupled to ground. It represents a low-pass filter causing a voltage drop over R_s	41
4.4	Signal over sensing resistor during acquisition, varying R_s , for an amplitude of the square wave of 0.83 V.	43
4.5	Signal over sensing resistor during acquisition, varying R_s , for an amplitude of the square wave of 2.07 V.	44
4.6	Signal over sensing resistor during acquisition, varying R_s , for an amplitude of the square wave of 2.70 V.	45
4.7	Signal over sensing resistor during acquisition, varying R_s , for an amplitude of the square wave of 2.90 V.	46
4.8	Signal over sensing resistor during acquisition, varying R_s , for an amplitude of the square wave of 3.3 V.	47
4.9	Signal over sensing resistor during acquisition, varying the signal amplitude, for $R_s = 1 \Omega$	47
4.10	Signal over sensing resistor during acquisition, varying the signal amplitude, for $R_s = 5.1 \Omega$	48

4.11	Signal over sensing resistor during acquisition, varying the signal amplitude, for $R_s = 10 \Omega$	48
4.12	Signal over sensing resistor during acquisition, varying the signal amplitude, for $R_s = 20 \Omega$	49
4.13	Signal over sensing resistor during acquisition, varying the signal amplitude, for $R_s = 100 \Omega$	49
4.14	Acquisition showing the ADC input signal, performed with the INA213. From 0 to 10 s, the user is not touching. From 10 s to 20 s he is touching the signal electrode. the cycle is repeated until 60 s are reached. $R_s = 1 \Omega$ and signal amplitude of 830 mV. . .	50
4.15	Acquisition showing the ADC input signal, performed with the INA213. From 0 to 10 s, the user is not touching. From 10 s to 20 s he is touching the signal electrode. the cycle is repeated until 60 s are reached. $R_s = 1 \Omega$ and signal amplitude of 2.48 V. . .	50
4.16	Acquisition showing the ADC input signal, performed with the INA213. From 0 to 10 s, the user is not touching. From 10 s to 20 s he is touching the signal electrode. the cycle is repeated until 60 s are reached. $R_s = 1 \Omega$ and signal amplitude of 3.3 V. . .	51
4.17	Acquisition showing the ADC input signal, performed with the INA213. From 0 to 10 s, the user is not touching. From 10 s to 20 s he is touching the signal electrode. the cycle is repeated until 60 s are reached. $R_s = 1 \Omega$ and signal amplitude of 3.3 V. . .	51
4.18	Touch detection signal with $R_s = 51 \Omega$ and signal amplitude of 2.48 V. The signal filtered by a moving average ($N = 10$) is superimposed, in red. The touch detection algorithm result is shown in the second plot.	52
4.19	Touch detection signal with $R_s = 10 \Omega$ and signal amplitude of 3.30 V. The signal filtered by a moving average ($N = 10$) is superimposed, in red. The touch detection algorithm result is shown in the second plot.	52
4.20	Schematic of the RX module.	53
4.21	Schematic blocks representing the link between the TX/RX and the signal electrode using two electronic switches sw1 and sw2 and one capacitor C.	54

4.22	Schematic blocks representing the link between the TX/RX and the signal electrode using two relè r1 and r2 and two different capacitors C1 and C2.	55
4.23	Previous <i>Live Wire</i> RX user recognition system. A difference in the path to ground impedance is exploited, switching between three pin: the first one at half power supply potential ($V_{DD/2}$), the second linked to the RF front-end and the third one directly to ground. . .	56
4.24	Representation of the RX electrodes directly in contact with the skin. The first one represents the RX signal electrode while the second one allows to increase the ground coupling, by coupling the receiver to the human body. The electric model is reported below. .	57
4.25	TX ADC signal acquisition while the RX relè switches between ground and RX front-end at 1 Hz. The RX electrode was placed on the right forearm while the right hand was touching the TX signal electrode. The RX ground electrode was placed on the left forearm, increasing the distance "d" as much as possible.	58
4.26	TX ADC signal acquisition while the circuit is swithing at 5 Hz between: ground and RX front-end - ground pulses at 1 MHz, for 200 ms.	60
4.27	Power supply block. 3V3 pin is an output pin from the PYBD, used to obtain the power sypply for the TX, the RX, the relè at TX stage, the relè at RX stage and the INA213.	62
4.28	WBUS-DIP 28 board with all its input/output pin. In the center, the two bus connectors are used to plug-in the board to the PYBD.	62
5.1	INA213 acquisition while subjects are sitting down, without shoes and without gloves, touching the microwave oven every 20 s for 10 s.	65
5.2	INA213 acquisition while subjects are sitting down, without shoes and with gloves, touching the microwave oven every 20 s for 10 s. .	66
5.3	INA213 acquisition while subjects are standing up, without shoes and without gloves, touching the microwave oven every 20 s for 10 s.	66
5.4	INA213 acquisition while subjects are sitting down, with shoes and with gloves, touching the microwave oven every 20 s for 10 s. . . .	67
5.5	INA213 acquisition while subjects are sitting down, with shoes and without gloves, touching the wardrobe every 20 s for 10 s.	68

5.6	INA213 acquisition while subjects are standing up, without shoes and without gloves, touching the wardrobe every 20 s for 10 s.	69
5.7	INA213 acquisition while subjects are standing up, without shoes and with gloves, touching the wardrobe every 20 s for 10 s.	69
5.8	INA213 acquisition while subjects are standing up, with shoes and without gloves, touching the wardrobe every 20 s for 10 s.	70
5.9	INA213 acquisition while subjects are sitting down, without shoes and with gloves, touching the drawers every 20 s for 10 s.	71
5.10	INA213 acquisition while subjects are sitting down, with shoes and with gloves, touching the drawers every 20 s for 10 s.	72
5.11	INA213 acquisition while subjects are standing up, without shoes and without gloves, touching the drawers every 20 s for 10 s.	72
5.12	INA213 acquisition while subjects are sitting down, with shoes and without gloves, touching the drawers every 20 s for 10 s.	73

Chapter 1

Introduction on Intra-Body Communication

Intra-Body Communication (IBC) is an innovative wireless and short-range communication method, which allows the human body to be used as a transmission medium thanks to its electrical properties. For frequencies lower than 20 MHz, it acts as an antenna due to the high value of the dielectric constant of the body. There are many surveys on Wireless Body Area Network (WBAN) applications; IBC offers a valid alternative as it makes communication safer and more specific. RF-based techniques, Zigbee or Bluetooth, act over a much greater distance, tens of meters, increasing consumption due to the power radiated into the surrounding environment with consequently low energy efficiency. For instance, Zigbee energy consumption is 109 nJ per received bit at 250 kbps, which corresponds to 26.5 mW of power consumption. At the same time, UWB requires 41.75 mW at 16.7 Mbps. On the other hand, IBC ensures a much greater energy efficiency [2].

IBC is based on near-field coupling, so the frequencies used, signal power, power consumption and device size are less, providing benefits in terms of external interference reductions and miniaturization [1].

Miniaturization itself is an essential factor that has to be considered, because more than one receiver device may be intended to be brought by the subject. Battery replacement may represent a critical issue especially in such applications that

involve medical healthcare. Hence the lower energy dissipation has to be considered one of the most significant advantages of IBC. Moreover, RF techniques need an on-body antenna, whose dimensions are proportional to the wavelength; so to exploit higher frequencies, a bigger antenna is required, increasing the size of the whole device.

Furthermore, at the frequencies of interest, the known health-related effects centered around human tissues have to be taken into account. The International Commission on Non-Ionizing Radiation Protection (ICNIRP) specifies limits and restrictions to ensure safety when time-varying electromagnetic fields irradiate the body. For frequencies in the range of 100 kHz - 10 GHz, the restriction is about the Specific Absorption Rate, the so-called SAR, representing how much energy has been absorbed by tissues when exposed to a radiofrequency electric field [W/Kg]. Typically, WBAN devices radiate less amount of power, so in this case, localized SAR has to be considered. It is the general Specific Absorption Rate in the radiated part of the body [3].

The body used as a transmission medium brings essential advantages compared to standard RF protocols as shown in figure 1.1, especially considering biomedical sensor networks exploited for continuous healthcare monitoring.

	IBC	RF (NB , UWB)
Communication Medium	Human Body	Air
Frequency Band	Centered at 21 MHz ($f_{BW} = 5.25$ MHz)	Different bands (402MHz-10GHz)
Data Rate	< 2 Mb/s	< 13 Mb/s
Transmission Range	< 2 m	10 m
Signal Attenuation	Low	High (Body Shadowing)
On-Body Antenna	No	Yes
Energy Efficiency	High (High Conductivity of the human body)	Low (Air has low conductivity)

Figure 1.1: Comparison between RF and IBC techniques.

When touching objects and sending information about their leading roles is the primary goal, intra-body communication represents the best solution because it is not affected by the crosstalk phenomenon. Therefore, digital information containing sensitive data can be transmitted by objects without any interferences [4]. Moreover, IBC offers other advantages over the other techniques, as communication is based only on the possible touch of the external object by the subject.

Originally, the idea behind IBC was to exchange information between multiple wearable devices on the human body, possibly connected to an external device. Subsequently, research focused on the human-external environment interface and making the exchange of data between a wearable device and surrounding objects effective and safe [5].

At the basis of this idea, there is the need to be able to offer technical support to people who have partially or totally lost their sight; for them, this communication system can be seen as an indoor navigation system and a possibility of interactive dialogue with household appliances and metal objects at home.

As it stands, IBC techniques represent a more efficient method to reduce power consumption and grant secure short-range communication compared to wireless RF. Although good results have already been achieved, many remaining challenges have to be dealt with: how the user motion can modify the transmission quality and improve it, how an increased data rate can be achieved using lower frequency carriers, and how a long-term use can affect the health of the user [2].

Chapter 2

State of the art: Intra-Body Communication and Radio Frequency

2.1 Radio Frequency Body Area Network

A Wireless Body Area Network (WBAN) usually consists of low-power, miniaturized devices characterized by wireless communication capabilities. These devices can monitor not only specific functions of the human body, but also properties of the surrounding region, enabling communication between these two different systems [3].

They can be divided into several categories according to their capabilities and exploited technologies. In the next sections, different techniques that represent an alternative to IBC will be discussed briefly, taking into account their advantages and disadvantages.

Most of the works in the literature focus on RF WBAN devices. They are often classified by the frequency range as shown in figure 2.1.

For frequencies between 420 MHz and 1.4 GHz, the system is called Wireless Medical Telemetry System (WMTS), and it represents one of the most used RF bands in biomedical applications. These RF frequencies are usually employed for implanted and on-body devices, which are based on point-to-point communication.

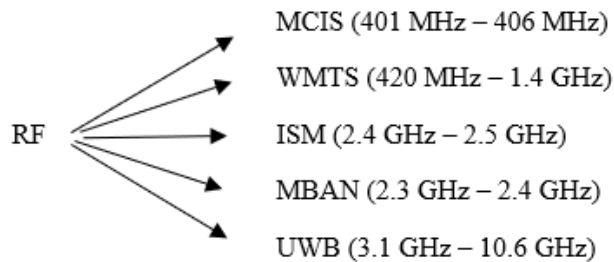


Figure 2.1: Taxonomy of RF techniques used for WBANs.

Because of these frequencies, it is possible to improve the bit rate and reliability, which represent a problem for magnetic coupling, a communication technique used in other types of devices.

Another option is represented by the Ultra-Wide Band (UWB). According to the IEEE 802.15 Task Group 6 standards, a UWB signal goes from 3.1 GHz to 10.6 GHz. UWB has been widely used because of some essential properties, making it a useful frequency range for these applications: its resistance to multi-path losses and interference, its very high bit rate (up to 500 Mbps). On the other hand, the main issue is represented by its energy consumption. For instance, at 10 Mbps, its power consumption is one order of magnitude higher than the IBC power consumption [3].

Generally, UWB devices are powered by batteries whose lifetime, according to medical applications, has to be of the order of some years. Hence it is necessary to grant a transceiver characterized by ultra-low power design.

Reducing the duty-cycle may represent the right solution to maintain the CPU and the transceiver turned off most of the time as the device goes in a sleep mode. However, if some applications need frequent transmission, this solution can not be considered.

The path loss obtained using either UWB or narrowband radio signals has been treated by several surveys. Both these kinds of studies highlighted significant losses. It is known that, in wireless networks, the transmitted power decreases with d^η where η represents the path loss coefficient (the aka propagation coefficient, e.g., for free space η is equal to 2) and d the distance between the transmitter

and the receiver. Usually, also other kinds of losses are considered, such as the fading signal due to multi-path propagation [6].

In general, there are two main types of propagation, according to where it happens:

- **In the body:** when signal propagation happens in the human body, losses are mainly caused by the power absorption inside the tissue. This power will then be dissipated as heat. The already discussed SAR is the standard measure of how much power has been absorbed; the path loss is much more significant than observed in free air due to the great amount of water inside tissues. In particular, a difference of 30-35 dB compared to free air at a short distance is noticed. The most critical issue brought by the propagation of an RF signal inside the human body is the increasing temperature, which can easily damage human tissues [6].

Table 2.1 shows the cell damage at different temperatures and for a different time.

Biological effect	Necessary physical effect	Temperature range	Exposure time
Cellular growing	No effects	30-39	—
Increasing of perfusion. Hyperthermic death	Variations of tissue optic properties	40-46	30-60 min
Proteic denaturation	Necrosis, coagulation	47-50	> 10 min
Cellular death	Necrosis and coagulation	>50	after 2 min
Proteic denaturation, membrane disruption and cellular shrinkage	Coagulation, ablation	60-140	A few seconds

Table 2.1: Biological effects due to an increase of temperature.

- **Along the body:** The path loss along and around the human torso has been studied by Braem et al. [6]. Two different situations have been discussed in this survey: the propagation along the line of sight (LOS) of a phantom torso

and along a non-line of sight (NLOS). In the first case, the physiological curvature effects are not taken into account for the simulations [6].

Simulations with different signal frequencies have been performed, particularly the first one using UWB signals, with frequencies between 3 GHz and 6 GHz, and the second using a narrowband system at around 2.4 GHz. It has been found that results in the second case are very similar to those obtained using a 3 GHz signal. The path loss η is between 3 and 4. This difference is due to the position of the device. If it is placed on the arm, η is lower than the path loss when the device is on the trunk. Probably this is due to the much greater volume of the trunk, which implies a higher absorption.

For the NLOS situation, the EM field diffracts around the body and has no direct path through the body. A path loss between 5 and 6 has been calculated in this situation, so more than twice than that one for LOS [6].

In figure 2.2, different results for the path loss in LOS and NLOS settings are shown as a function of the distance d . They clearly show how the η value for NLOS is higher than the opposite case.

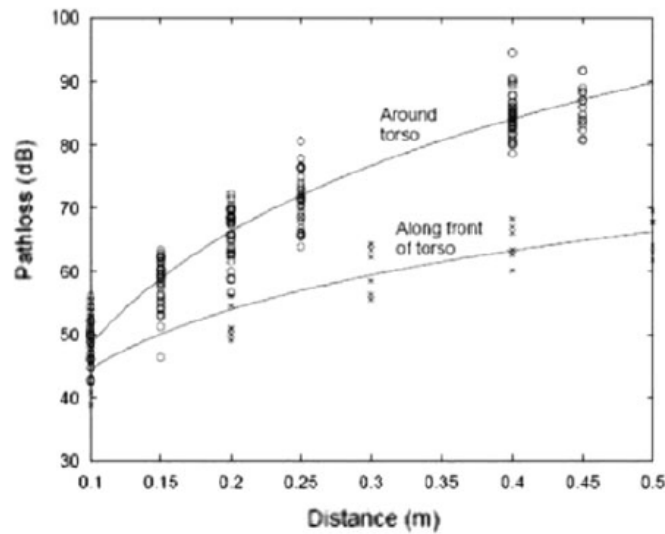


Figure 2.2: Measured path loss as a function of the distance around the torso (NLOS) and along the torso (LOS). A lower path loss characterizes Line-of-sight communication.

2.1.1 ZigBee

Bluetooth is a well-known and influential technology that allows high communication bandwidth. It can quickly arrive until 720 kb/s. Although Bluetooth can work minimizing its power consumption, protocol stack implementation complexity and constraints represent a limit for WBANs.

ZigBee assumed a key role in wireless technologies and is one of the most essential and diffused communication standards. It exploits digital and tiny antennas characterized by one of the lowest power consumption that makes it suitable for many applications in Wireless Sensor Networks.

ZigBee uses radio frequencies for industrial, scientific and medical aims, the so-called ISM, which can assume different values depending on the country and the region in which it is exploited. For example, it works at 868 MHz in Europe and 915 MHz in the USA, but today the only proper implementations available on the market are those at 2.4 GHz. This technology was created to be simpler and cheaper than other Wireless PANs such as Bluetooth.

ZigBee is usually employed for embedded applications that require low power consumption and transfer rates. It can grant a 250 kb/s transfer rate, making it one of the best solutions for applications in the medical field and wearable devices. The goal of ZigBee is to represent a non-targeted, economic and self-managed wireless mesh network, which will have such low energy consumption that it can operate for one or two years using the battery incorporated in the individual nodes. In general, the ZigBee protocols support both "beacon-enabled" and "non-beacon enabled" networks; they minimize the radio transmitter activity time, thus reducing energy consumption.

In beacon-enabled networks, nodes consume energy only in the period in which the beacon is present. However, in non-beacon enabled ones, most of them continue to consume because they are practically always turned on [7].

Zigbee technologies make available three different types of devices:

- **ZigBee Coordinator (ZC):** it represents the most complete and "intelligent" unit among those available because it constitutes the first element of the ZigBee chain, it can act as a bridge between multiple network elements.

Only one "Coordinator" can be present within a ZigBee network and it is also capable of storing information about its entire network.

- **ZigBee Router (ZR):** these devices act as intermediate routers allowing data transmission in both directions: from and to other devices. There are no hardware distinctions between a ZC and a ZR except that the role of initializing the network is released to the coordinator.
- **ZigBee End Device (ZED):** they include only the minimum functionalities to communicate with the parent node (ZigBee Coordinator), for these units it is impossible to transmit data to and from other devices, hence they do not participate in the multi-hop of a message; they are the nodes that require the lowest amount of memory and their cost is lower than the others ZigBee devices.

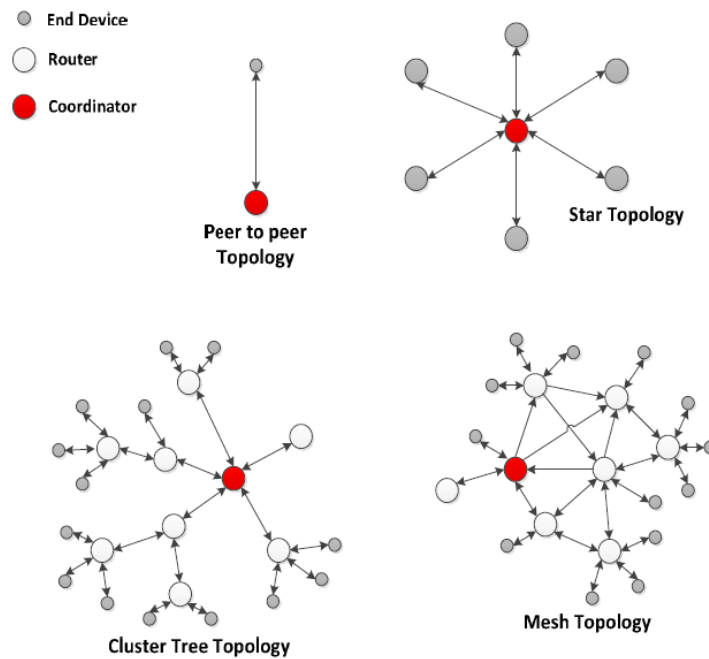


Figure 2.3: Different Zigbee topologies: Peer-to-peer, star, cluster tree and mesh topology, each one based on the use of three ZigBee devices: a coordinator, a router and an end device.

Figure 2.3 shows different ways in which a ZigBee topology can be built, starting from the three Zigbee devices dealt. It has to be noticed that routers are always in a

central position between coordinator and end devices, like coordinators themselves. There are not any hardware differences between these two categories.

2.1.2 Beacon

Beacon technology, based on Bluetooth, allows communication in a short distance between a transceiver and a receiver. Bluetooth beacons are characterized by low energy consumption and a wide propagation pattern, which means that the signal can be taken in a big range of distances from the transceiver.

Its versatility represents the first benefit of this technology: the user can wear the receiver on every part of his body without affecting the effectiveness of the transmission. On the other hand, using many beacon communication lines simultaneously, crosstalk may occur; the proximity of many objects working simultaneously results in signal crosstalk that makes difficult their correct pinpointing. In this scenario, there could be an information distortion, reducing the device effectiveness. Furthermore, this is a less safe method than the others because the communication does not happen only when the user requires it or when a specific action has been performed, not guaranteeing user privacy and data security.

Figure 2.4 shows how the Intra-Body Communication device dealt in this thesis, the *Live Wire*, represents a better solution concerning signal propagation. As shown, it remains fixed to the object irradiated by the transceiver, granting low power consumption and security for the user.

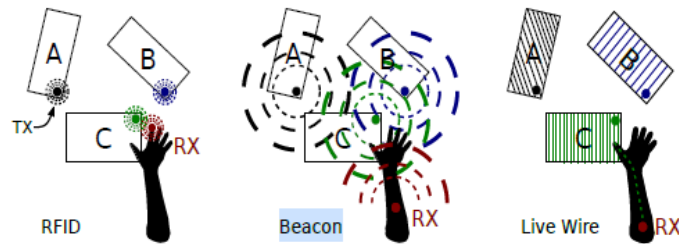


Figure 2.4: Comparison between RFID, Beacon, and *Live Wire*, regarding the propagation of the signal around the TX node.

2.2 Intra-Body Communication

As it can be seen from the previous section, IBC allows to overcome some limitations of each of the other techniques, so during last years, this technology became the object of many surveys, resulting in the release of different products and demonstrators.

For instance, Microchip released BodyCom, a short-range, low-data-rate communication system that can be connected to many wireless devices. It provides a bidirectional full-duplex communication by exploiting two different channels operating at different frequencies. It exploits a capacitive coupling for up-link and down-link to a base-station at 8 MHz and 125 kHz, respectively, enabling communication and data transmission from a wearable tag. Intra-Body Communication uses the human body to obtain a close loop circuit. This asymmetric link can reduce power consumption at the receiver node but not at the transceiver node, which has to deliver more energy because the human body attenuates the signal at frequencies around hundreds of kHz.

In figure 2.5 the BodyCom system is represented: the signal transmission uses a low frequency near field communication channel between the human body, the base unit (BU) and the mobile one (MU).

Due to the low-frequency range employed, the signal results attenuated, requiring a higher amplitude to be transmitted. It can be possible because the transceiver, the BU, represents a fixed device so that it can take power externally or from a battery. Thus, it can deliver a more significant amount of energy and the selected signal generated by the base unit has a frequency of 125 kHz. On the other hand, to reduce consumptions, the MU can be powered by a battery. For this reason, it is a wearable device [8].

In this system, the communication starts from the BU. The communication must begin only when the BU is coupled with the MU on the human body. Hence, the microcontroller continuously performs touch detection, so it checks if the user is touching the transmitter node in a loop. If a touch has occurred, it stops this loop and starts the transmission [8].

Figure 2.6 shows blocks diagram for the base and mobile units. A microcontroller manages the BU and the hardware includes the required circuitry to transmit the signal and a visual interface to allow the user to interact with the device. It is

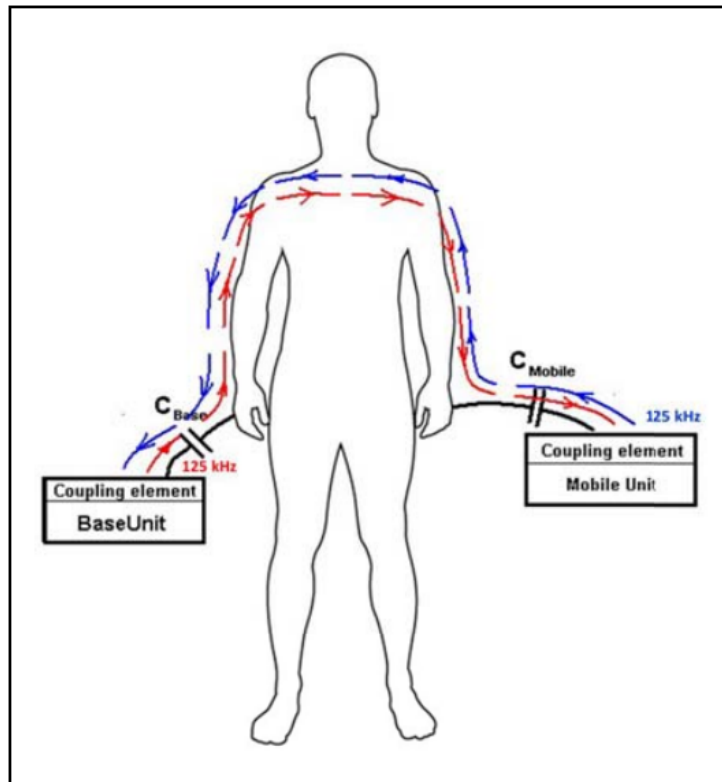


Figure 2.5: BodyCom system working principles.

essential that both the BU and the MU can send information and elaborate and process the received ones.

Figure 2.7 shows the mobile unit state diagram highlighting all the device software features.

In comparison with all the other technologies, BodyCom improves security because of the possibility to perform a full-duplex communication between the BU and the MU. Moreover, it provides energy usage due to the possibility to communicate only if touch occurs. Compared to the other techniques, such as beacons and proximal sensors, it ensures privacy and is not affected by crosstalk. The aim is to provide information exchange only if objects are intentionally touched, for instance, to interact with home appliances or small objects in general. Typically, this purpose has been done using Braille labels. However, this technology can overcome the limits of using these tags for large objects because an active extensive tactile exploration is required, which may be quite uncomfortable for blind or

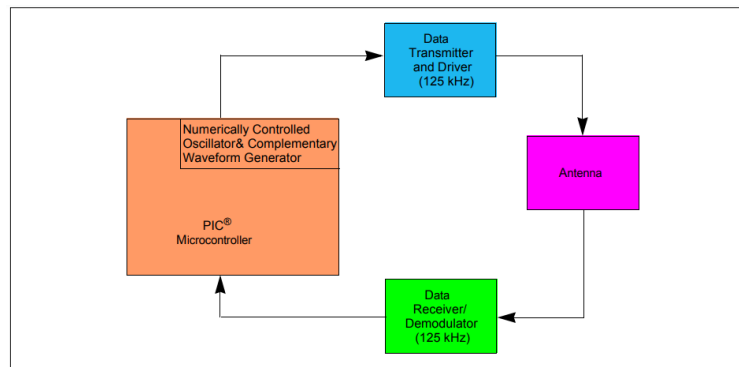


Figure 2.6: Representation of the device working steps. Mobile/base unit block diagram.

visually impaired people.

In 2008, Ericsson launched Connected Me, an Intra-Body Communication based on system that enables multimedia and/or data transmission as well as private information exchange while people handshake [4].

Marco Crepaldi et al. [5] focused their research on the implementation of a low-complexity and low-cost Intra-Body Communication system suitable for a human-to-environment extension which is also characterized by voice-assistance and home integration. *Live Wire*, is a non-coherent (TX to RX connection) kHz-range threshold-based and impulse-radio system which works thanks to haptic interactions with objects. It has been thought to be developed using mainly low-cost components, fully programmable and easily to install [5].

It exploits the quasi-static near-field, the low-frequency electric field approximation of the human body, and the transmitter direct path to ground. For this reason, it can be attached to any conductive object with any possible shape, requiring a shallow current.

The *Live Wire* main function is identifying landmarks for visually impaired people who may use this device as indoor navigation and object interaction system, allowing a sightless person to quickly get information from the surrounding environment only by touching an object. This represents the key point of this technology: the digital information is confined to the haptic enclosure.

It has to be considered that there are many surveys in the literature that study

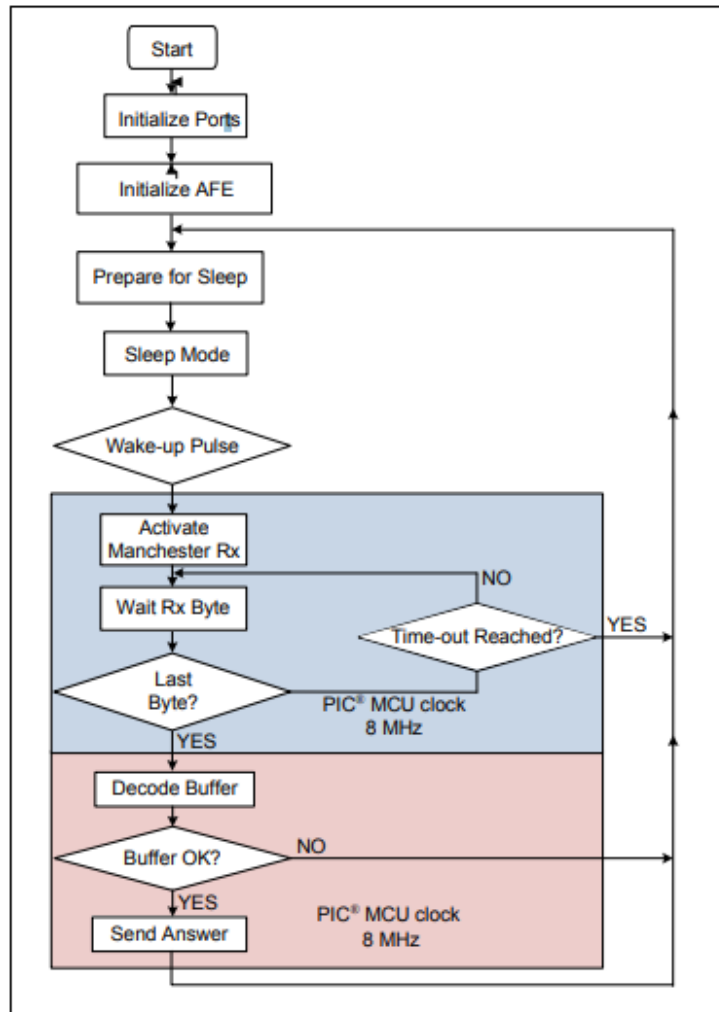


Figure 2.7: Representation of the device working steps. Mobile unit state diagram.

navigation systems. It is a well-known and trained process, but landmarks identification is not.

Figure 2.8 presents a typical example of how the user can use the device. The upper part of the figure shows the electrical circuit in which the TX low impedance path to ground and the RX high impedance path to ground, capacitive coupled, are highlighted. The user can theoretically wear the receiver where he wants. It has not to be placed in proximity of the object, not even in contact with the skin, as discussed more thoroughly in the next sections.

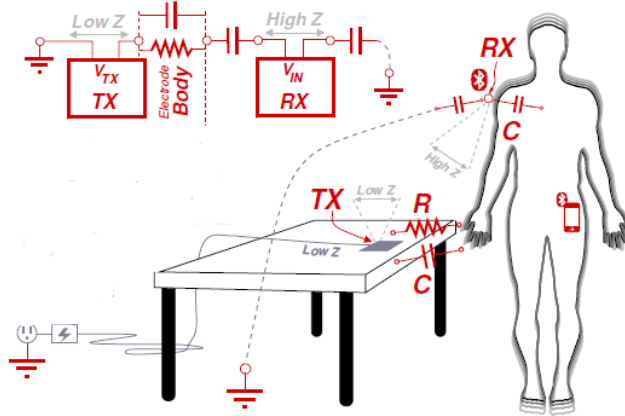


Figure 2.8: *Live Wire* architecture: the TX attached on the table is directly linked to ground and the RX can capacitively close the circuit to ground, thanks to the high impedance path.

A variety of IBC techniques have been proposed, and more in general, all of them can be classified into three main groups:

2.2.1 Capacitive coupling

IBC was treated for the first time in 1995 by Zimmerman [9], a student of Massachusetts Institute of Technology (MIT), and other researchers. They developed a system in which a transmitting electrode was mounted close to the human body performing a capacitive coupling, so without any touch occurs, with a receiving electrode. To close the circuit, another couple of electrodes is necessary. It was used to perform the ground coupling. This novel and innovative method to communicate exploiting the human body was called capacitive coupling Intra-Body Communication. Zimmermann used as input signal a 330 kHz wave transmitted through the body, then received by the receiving electrode. The power consumption was very low, around 1.5 mW and the transmission rate was about 2.4 kbit/s. In figure 2.9 the Zimmerman model for capacitive coupling Intra-Body Communication is represented. It is shown the couple of electrodes that can be in contact with the body, ensuring the current flow; the other two electrodes have to be connected/coupled to ground.

The system was composed by three main components: the transmitting termi-

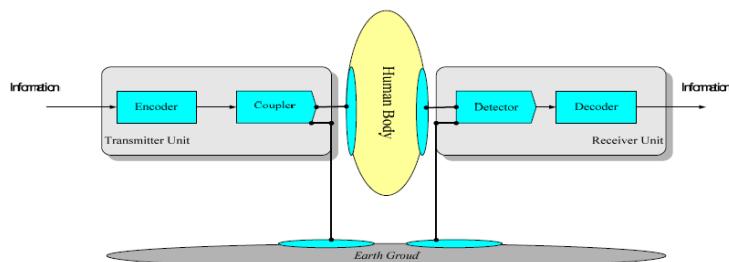


Figure 2.9: Zimmerman intra-body communication model.

nal, which was the node from which the signal was first generated, then sent, the receiving terminal, which should collect the signal, and the human body, which allowed the communication between these two terminal closing the circuit. Hence the use of a signal electrode for the transmission and detection of signals was necessary; moreover a grounding electrode was used, it should close the circuit to ground.

Zimmermann has been the first, but after him, many surveys focused on this novel and innovative technique: M.Gray et al. [10] designed a device, starting from the idea developed by Zimmermann, which used a 100 kHz signal and increased the maximum theoretical bandwidth to 2000 kbps. It has been shown that the first causes of noise are the amplification stage and the electromagnetic interference due to the external environment. Then a half-duplex communication, characterized by a 9600 baud transmission rate. was achieved and integrated into the device; this represents a key-point because the energy transmission and the data transmission are enabled and performed with this Intra-Body Communication system.

Subsequently, the transmission rate has always been improved, making devices faster and maintaining low energy consumption. K Partridge et al. [11], obtained a transmission rate of 38.4 kbit/s in which the FSK modulation mode at 180 kHz and 140 kHz carrier frequencies was used. Many experiments concerning tunings of signal parameters were carried out: different voltage (with the maximum of 22 V), different transmission rates and other communication indexes have been evaluated. These tests showed that the appearance of a ground electrode on the transmitter or the receiver had effects on the signal. However, it was susceptible

to the distance between the electrodes, the transmitter, and the human body-receiving electrode. Moreover, there was a robust signal attenuation due to the reduced ground plate size.

The Nippon Telegraph and Telephone [12] developed in 2004 the ReadTacton, it was the first practical IBC application based on capacitive coupling. For the first time since Zimmerman treated Intra-Body Communication, a transmission rate of 10 Mb/s was obtained. Later, Sony Corporation and China University developed another IBC device, the Wearable ID Key.

Since the Korea Advanced Manufacturing Research Institute [13] proposed an accurate electric circuit for the RC model of the human body, IBC studies became more accurate. These novel body models could be considered consistent with human experimentation within the range of 100 kHz - 150 MHz, which covers the whole range used for IBC devices and applications [14].

2.2.2 Galvanic coupling:

In this type of coupling, the signal is applied differentially between two transmitting electrodes and received by two receiving electrodes in a differential mode. In this situation, the signal is confined within the body and it is more robust to noise from the external environment.

In its studies on galvanic coupling for Intra-Body Communication, Handa et al. [15] placed a monitoring device, an electrocardiogram, and a receiving electrode on the chest and the wrist of a subject. The electrocardiogram signal electrode sent a weak current collected by the receiving electrode on the wrist through the human body, achieving signal transmission. An AC current of 20 μA has been used to transmit the signal through the body. Both transmitting and receiving electrodes have to be always in contact with the skin, which can be considered a resistor [14].

This Intra-Body Communication coupling setup can be analyzed in figure 2.10. Three different components are highlighted in the scheme: the transmitter unit, the receiver unit and the human body. Electrodes have to be directly in contact with the skin. The main difference between galvanic and capacitive coupling is that the first one does not require a ground coupling because the signal can return thanks to the second receiver and transmitter electrodes. In this way, there are no

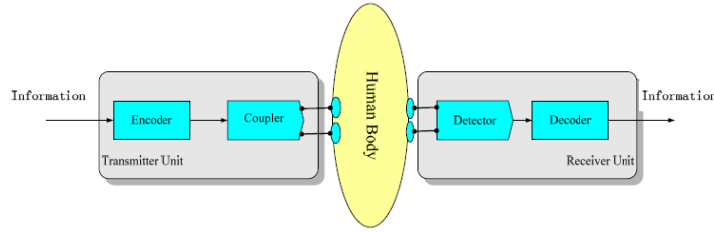


Figure 2.10: A galvanic coupling scheme for Intra-Body Communication is represented. The human body can be considered, in first approximation, a resistor. Receiving and transmitting electrodes are attached to the receiver and transmitter units, respectively, to encode the information in an AC current signal and decode after collecting it.

issues regarding the devices placing according to maximize the ground coupling of the circuit. The only factor that has to be taken into account is to put electrodes in the optimal location and to keep them in contact with the skin.

The advantage lies in a lower power consumption. The developed device is characterized by only $8 \mu\text{W}$ of power consumption. All these factors allow to use this technique, especially for an implantable device that can exploit Intra-Body Communication; on the contrary, a capacitive coupling may be difficult to be implemented for such applications because of the necessary ground coupling [14].

Galvanic coupling based on IBC can be divided into four main communication modes according to the receiver and transmitter position in the human body. The next subsections will show some examples of these different communication systems. It will be discussed in particular, the attenuation of each communication mode. For galvanic coupling, the attenuation is:

$$\text{Pathloss}(\text{dB})_{galv} = 20 \log_{10} \frac{V_{RX}}{V_{TX}}$$

Which is different from the same in the case of capacitive coupling:

$$\text{Pathloss}(\text{dB})_{galv} = 10 \log_{10} \frac{P_{RX}}{P_{TX}}$$

"Surface-to-surface" communication:

The receiver and the transmitter are placed on the human body, in contact with the skin. In this way, the surgery is unnecessary, and the installation steps are easily to be performed. Since Handa T. et al. [15] introduced the galvanic coupling Intra-Body Communication, D.P. Lindsley et al. [16] used the human body as a transmission medium for electric signal resulting in a novel method to measure the tension along the fore cruciate ligament. Different tests have been performed to find the most effective configuration, comparing different carrier frequencies and currents. The best setup for this measurement consisted of a 3 mA current signal at 37 kHz.

Starting from these results, K.Hachisuka et al. [17] proposed another novel communication, the waveguide-mode Intra-Body Communication. According to this technique, the human body can be considered a tube that allows the high frequencies electromagnetic waves flow sent by the transmitter.

Oberle [18] from the Swiss Federal Institute of Technology in Zurich developed a simple set of devices that could produce alternating currents of the order of some mA, based on the dielectric properties of the human tissues in which the signal should pass through.

On these bases, Wegmuller [19] built a model for the signal attenuation of the forearm, highlighting the effects of electrodes size and position; to perform this preliminary finite element model, he used waves of 10 kHz and 1 MHz, orthogonal current of 1 mA obtaining a transmission rate of 4.8 kbit/s.

"Surface-to-implant" communication:

This type of communication is often used to allow energy transfer from an external device to an implantable device placed within the tissue at a certain depth under the skin. In this case, the transmitter device is the external one, placed directly in contact with the body. It sends the signal through the skin and the tissues to the receiver electrodes, under the skin, to achieve communication.

Z.D. Tang [20] proposed to use this communication system to transfer external energy to the implantable devices, providing power supply for electronic components. His study focused on the way to exploit biological tissues volume conduction characteristics to provide communication. An equivalent circuit has been used to

simulate the skin-electrode, to analyze the amount of energy delivered by the system, the X type (with explicit physical significance).

Simultaneously, the impedance and voltage ratios of the output loop have been obtained through circuit analysis. Tang used pig skin to perform his experiment: a 2.8 mA current was used and the corresponding transmission efficiency achieved was the 27 %. On the other hand, the energy transmission efficiency was lower, the 11 %.

Therefore it has been proven that energy transmission from an external to an implanted device by virtues of biological tissues volume conduction characteristics can be obtained. Moreover, considering the transfer functions of different tissues, a tuning of the signal frequency can be performed in order to maintain the efficiency as high as possible and to maximize the energy delivered by the transmission system.

"Implant-to-surface" communication:

This communication method represents the opposite situation of the previous one. The implanted device sends a signal which will be exploited to obtain current coupling through the human body to allow information exchange. The main difference is that for "implant-to-surface communication", the external device position can be modified in order to maximize the signal transmission, so minimizing path losses. In other words, the surface device position can be seen as a function of the received energy and this function has to be maximized. It is important to note that the energy loss due to the transmitter outer position, in this case is avoided because of its inner position. On the contrary, in the previous case, the efficiency of the method was affected by the environment around the surface device, which causes higher energy losses and reduces the signal intensity at the receiver node. Lindsey [16] performed a tension measurement on a dead body's ligament. The communication was allowed by converting the tension into a current and then transmitting this signal to the surface electrode placed on the leg. Electrodes of 0.38 mm of diameter placed at a distance of 2.5 mm have been used, with a set of electromyography electrodes placed on the leg surface. The signal was a 3 mA sinusoidal with the carrier waves of 2-160 kHz, which produced a signal attenuation of 37 dB because during an EMG measurement, signal can be affected by many factors, including electrodes distance, electrodes size, depth of signal generation.

Sun et al. [21] proposed a different solution in which they used an antenna as transmitter at the implant node; in this way, a more extensive current range can be generated so that the surface implant can collect a higher current. Two different types of experiments have been performed: first, with the saline water, in which the antenna needed only a tiny amount of power (only the 1 % of the usual electrode couple amount), and with a sedated pig. Due to the antenna diameter, around 9 mm, the system did not cause big injuries to the pig's brain.

"Implant-to-implant" communication:

In this type of communication, two different devices, both implanted, send each other information through human tissues. The first advantage is represented by the absence of the external environment, which increases losses around the transmitter. For this reason, the effective power is higher, and the power consumption and signal attenuation are lower than the other techniques in which the transmitter is on the body. Moreover, it is lower than implant-to-surface communication as well. Additionally, one of these two implanted devices can send the signal to an external one exploiting connecting lines or wireless RF.

Wegmuller et al. [22] proposed an implant-to-implant communication system in which they simulated communication between two couples of electrodes, receiving and transmitting, on a simulated muscular human tissue. The frequency range was from 100 kHz to 500 kHz and the current amplitude was below 1 μ A. Many tests using different electrodes to compare signal attenuations have been performed. For this reason, two types of receiving and transmitting electrodes have been designed: exposed copper cylindrical electrodes, characterized by a length of 10 mm and a diameter of 4 mm, and exposed copper coil with a diameter of 4 mm; the distance between them was 50 mm. Tests highlighted that the signal attenuation was much more significant using the cylindrical electrodes than the coil electrodes. In the first case, it was around 32 dB within 50 mm, while it was around 47 dB with the second one. Different electrodes cause a very different result in terms of signal attenuation.

Al-Ashmouny K.M. et al. [23] developed a system in which one electrode among the two transmitting ones and one among the two receiving ones are not directly in contact with the skin. The system was tested on a stupeficient mouse: electrodes

were placed within the mouse brain. This system exploits a high signal transmission rate because the transmitting module's receiving circuit is insulating, causing a larger communication mode impedance ratio.

The system should avoid charge accumulation in order to avoid tissue injuries. For this reason, a steady AC signal has been used for the scope. An attenuation of 20 dB has been reported. A high signal transmission rate characterizes the system but, on the other hand, the current emitted by the receiver can easily affect it. If the circuit is closed to ground by a low impedance conductor, the human body is directly in contact with the ground and the signal decreases rapidly [14].

2.2.3 Waveguide methods:

While the first two groups use lower frequencies, lower current and voltage levels, this technique exploits an electromagnetic wave that propagates through the body, involving a non-negligible radiation component into the air. Thus higher frequencies have to be used, increasing power consumption [1].

Chapter 3

IBC theoretical background

3.1 Dielectric properties of materials and human tissues:

Electrical characteristics of materials, including biological tissues, present different behaviors. They can be separated into two main categories: insulators (or dielectrics) and conductors. For dielectrics, charges can not move freely and they remain fixed in their position. On the contrary, for conductors, electric charges can flow if an electric field is applied [24]. Considering an electric field applied on a conductor, it allows charges to move until it becomes equal to zero. For polar materials, negative and positive charge centers do not coincide. For this reason, a dipole moment p is generated as an electric field occurs. Hence, positive and negative charges tend to follow different directions according to the more positive or negative value of the electric field; this phenomenon is called polarization and generates a second electric field in response to the application of the first one within the material.

Given the applied electric field E and the produced field into the dielectric material due to polarization E_P which has opposite direction of the first one, the net total electric field inside a material E , is:

$$E = E_0 - E_P \quad (3.1)$$

It has to be noted that the electric field E_P is higher if the material is an insulator, so it significantly lowers the total electric field E . Instead, if the material is a

conductor, the polarization effect does not occur because free charges can move freely. The reduction of the electric field obtained for insulators can be expressed by the dielectric constant, or relative permittivity ϵ_r

$$E = \frac{E_0}{\epsilon_r} \quad (3.2)$$

In practice, many materials, including biological tissues, are characterized by both conductive and dielectric behavior. There are free charges that can move within them and fixed ones that can rotate or take position according to the direction of the applied electric field, remaining fixed and causing an internal charge separation and storage. For this reason, we describe materials as having a conductivity σ and a permittivity ϵ , on a macroscopic point of view [25]. In free space $\epsilon_0 = 8.85 \cdot 10^{-12}$ F/m.

In general,

$$\epsilon = \epsilon_r \epsilon_0 \quad (3.3)$$

The behavior of a generic material, with a thickness d and a cross-section A , which presents conductive and dielectric properties, is determined by a capacitance

$$C = \epsilon A/d \quad (3.4)$$

and by a conductance

$$G = \sigma A/d \quad (3.5)$$

For these real materials, like human tissues, a simple model is the "Debye-type" in which a capacitor is in parallel to a resistor. So applying a DC voltage, there will be a conduction current equal to the product of the tension V and the conductance G ($I_c = GV$) and a charge equal to the product of the capacitance C and the voltage ($Q = CV$) will be stored by the capacitor. Considering an AC voltage

$$V_{(t)} = V_0 \cos(\omega t) \quad (3.6)$$

V_0 is the voltage amplitude, ω is the angular pulsation and it is equal to $2\pi f$ where f is the the voltage signal frequency. There will be also a displacement current due to the charging/discharging phenomenon on the capacitor plates

$$I_d = dQ/dt = -\omega CV_0 \sin(\omega t) \quad (3.7)$$

So the total current is given by the sum of I_d and I_c . These two terms are 90 degrees apart in phase. This phase difference is usually expressed by writing

$$V_t = V_0 e^{i\omega t} \quad (3.8)$$

Where

$$i = \sqrt{-1} \quad (3.9)$$

And taking into account only the real part. The total current is given by the sum of the conduction and displacement current, hence

$$I = GV + C \cdot dV/dt = (\sigma + i\omega\epsilon)A \cdot V/d \quad (3.10)$$

Physically, considering any material, we can consider the permittivity ϵ as "*a measure of the ability of dipoles to rotate or its charge to be stored by an applied external field.*" [26] and the conductivity σ as "*a measure of the ability of its charge to be transported throughout its volume by an applied electric field*" [26].

It is essential to highlight that if the conductivity and the permittivity remain constant, I_d increases with the frequency and I_c is constant because it is not a function of frequency. Therefore at low frequency, the conductive effect is much more significant and the material can be considered a conductor; while frequency increases, capacitive effects become more important. Moreover, these material properties are frequency-dependent, so changing the frequency of the electric field, or the applied voltage, σ and ϵ change as well; this phenomenon is called dispersion.

At low frequencies, dipoles can quite easily follow voltage changes and the electric field, so polarization occurs. At the same time, charge carriers can flow longer in the same direction before E changes its sign. For these reasons ϵ is higher and σ is lower. Increasing the electric field frequency, dipoles can not follow the rapid voltage changes anymore, so the polarization effect is gradually lost. On the other hand, charge carriers make even shorter distances before E changes its polarity again. Similarly, increasing the frequency, ϵ decreases because polarization disappears and the conductivity increases [27].

The dispersion phenomenon can be represented and quantified by its angular relaxation frequency or by its relaxation time

$$\omega_r = 2\pi f_r \quad (3.11)$$

$$T_r = 1/f_r \quad (3.12)$$

In figure 3.1 [28], both permittivity and conductivity as functions of frequency are shown. According to different frequency ranges, many dispersion regions are defined for permittivity. For frequencies lower than 10 kHz, the α dispersion is due to ions polarization along the cell membrane. In the MHz frequency range, the β dispersion: it takes origin from interfacial polarization of cell membrane. In fact, it does not enable the passive ion flow from inner to outer cell space and vice versa. Another reason that justifies the β dispersion is the polarization of proteins and other organic molecules at these frequencies. At frequencies of the order of GHz, the γ dispersion is due to the polarization of water molecules.

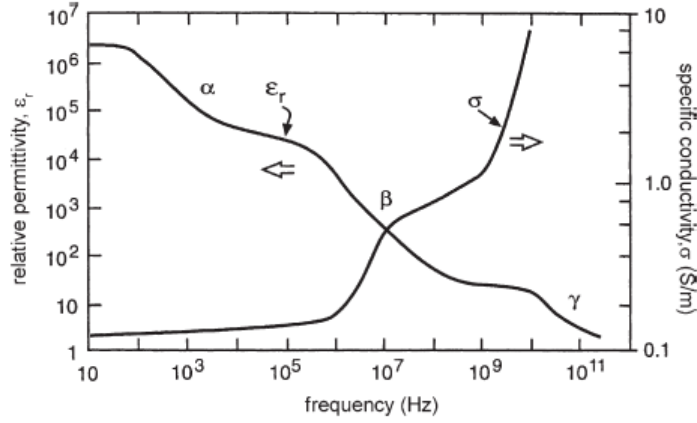


Figure 3.1: Typical permittivity ϵ and conductivity σ behavior as frequency-dependent functions. ϵ decreases with the frequency as σ increases. α , β and γ dispersion regions are highlighted.

Materials behavior can be analyzed by considering the displacement and conduction currents ratio $I_d/I_c = \omega \cdot \epsilon/\sigma$. At low frequencies, the ratio is low as well. In this condition, tissues are nearly conductive, although the increasing permittivity. As the frequency increases the ratio decreases.

According to the Debye-type model, in which a RC parallel is used, we can consider dispersion as

$$\epsilon_r^* = \epsilon_\infty + \frac{(\epsilon_S - \epsilon_\infty)}{(1 - i\omega t)} - i\sigma_0/(\omega\epsilon_0) \quad (3.13)$$

And

$$\sigma^* = \sigma_\infty + \frac{(\sigma_0 - \sigma_\infty)}{1 - i\omega\tau} \quad (3.14)$$

ϵ_r^* and σ_r^* are the complex permittivity and conductivity. Furthermore, the time constant $\tau = 1/RC$; ϵ_∞ , ϵ_S and σ_∞ , σ_0 refer respectively to the relative permittivities and conductivities at frequencies well above and well below the dispersion [26].

For human tissues, the Debye-type response represents a good approximation; but generally, a more stable relation is given by the Cole-Cole empirical relations [29]

$$\epsilon_r = \epsilon_\infty + \frac{(\epsilon_S - \epsilon_\infty)}{(1 - (i\omega\tau)^\alpha)} - i\sigma_0/\omega\epsilon_0 \quad (3.15)$$

And

$$\sigma^* = \sigma_\infty + \frac{(\sigma_0 - \sigma_\infty)}{(1 - (i\omega\tau)^\alpha)} \quad (3.16)$$

Where α depends on the material properties; it is equal to 1 in the previous model and it decreases increasing the dispersion width.

3.2 Electromagnetic field - biological tissues interaction:

Given an electric field E which varies at a frequency f , the human body interacts with it by modifying its perceived value. In particular, by separating the electric field into its two components, tangential (E_t) and normal (E_n), considering a body immersed in an electric field and calculating the value of the field inside the human body, we will have for the tangential components

$$E_{t1} = E_{t2} \quad (3.17)$$

And for the normal components

$$\sigma_1 \cdot E_{n1} = \sigma_2 \cdot E_{n2} \quad (3.18)$$

Materials conductivity has already been discussed, especially for human tissues; it varies with frequency. Conductivity σ decreases as the frequency decreases, hence at low frequencies (below tens of MHz), the electric field can be considered

constant at the interface with tissues and throughout the human body, which can be considered a conducting wire. Therefore it can be taken into account the only *quasi-static field* [9]. On the other hand, if the frequency increases, the electric field E decreases as it travels through the human body.

Considering as a signal source an electric dipole placed in correspondence of the human body, we will analyze how the E field will spread over it

$$E_{\theta} = \frac{I \cdot dz \cdot k^3}{4\pi\omega\epsilon_0} i \left[\frac{1}{kr} - \frac{i}{(kr)^2} - \frac{1}{(kr)^3} \right] \sin\theta \cdot e^{-ikr} \quad (3.19)$$

I is the electric current, k is the wavenumber, ω is the angular pulsation, dz is the dipol infinitesimal length, ϵ_0 is the permittivity in a vacuum. If the distance r from the source of the field is small, then the dominant term is $(1/r^3)$, but if the distance increases and we pass from the near field to the far-field, this becomes more and more negligible and the term $(1/r)$ becomes the one that dominates the expression of the electric field.

The expression of the electric field modulus near the human body is [30]

$$\begin{aligned} |E_Z| &= 2k \left| \underbrace{(1 - u^2 + u^4)F \cdot \frac{e^{i(kr-\omega t)}}{r}}_{\text{surface-wave}} + \underbrace{\frac{i}{k} \cdot \frac{e^{i(kr-\omega t)}}{r^2}}_{\text{reactive-radiation}} - \underbrace{\frac{1}{k^2} \frac{e^{i(kr-\omega t)}}{r^3}}_{\text{quasi-static}} \right| = \\ &= 2 \left| k(1 - u^2 + u^4)F \cdot \frac{1}{r} + i \cdot \frac{1}{r^2} - \frac{1}{k} \cdot \frac{1}{r^3} \right| \end{aligned} \quad (3.20)$$

Where $(1 - u^2 + u^4)F$ is an attenuating function that depends on the frequency and the permittivity of the human body. In particular, the entire corrective term $(1 - u^2 + u^4)F$ is shown in table 3.1 as a function of frequency, together with relative permittivity and conductivity, and all the terms that appear in the surface-wave term [30]. Approximating the human body as a semi-plane with finite conductivity, we obtain the formula of the electric field as a function of the distance from the infinitesimal dimension dipole if the propagation occurs close to the human body and not in the air, as in the previous case.

Given the wavenumber k

$$k = 2\pi/\lambda = 2\pi f/v \quad (3.21)$$

Where v is the propagation speed of the wave in the medium, increasing the angular pulsation ω , proportional to the frequency (or the wavenumber k , also proportional to f) and at the same time the distance r , we pass from the near-field

to the far-field. Therefore at higher frequencies, the capacitive coupling is not very effective [31].

Frequency [Hz]	kr	Relative permittivity	Conductivity [S/m]	$ u $	$ F $	$ (1 - u^2 + u^4)F $
100k	0.002094	1119.2	0.00045	0.0299	0.9991	0.9982
200k	0.004188	1104.8	0.00105	0.0300	0.9991	0.9982
300k	0.006283	1090.5	0.00193	0.0302	0.9991	0.9982
400k	0.008370	1076.3	0.00304	0.0304	0.9991	0.9982
500k	0.010471	1062.0	0.00436	0.0305	0.9991	0.9982
600k	0.012566	1047.7	0.00585	0.0307	0.9991	0.9982
700k	0.014660	1033.4	0.00751	0.0308	0.9991	0.9981
800k	0.016755	1019.1	0.00930	0.0310	0.9991	0.9981
900k	0.018849	1004.9	0.01121	0.0312	0.9991	0.9981
1M	0.020943	990.76	0.01323	0.0313	0.9990	0.9981
2M	0.041887	857.96	0.03710	0.0330	0.9989	0.9979
3M	0.062831	745.66	0.06314	0.0346	0.9987	0.9976
4M	0.083775	653.83	0.08823	0.0362	0.9984	0.9973
5M	0.104719	579.21	0.11134	0.0377	0.9981	0.9970
6M	0.125663	518.30	0.13226	0.0391	0.9979	0.9966
7M	0.146607	468.16	0.15109	0.0405	0.9976	0.9963
8M	0.167551	426.46	0.16806	0.0419	0.9972	0.9959
9M	0.188495	391.41	0.18339	0.0432	0.9969	0.9956
10M	0.209430	361.66	0.19732	0.0444	0.9966	0.9952
20M	0.418870	209.22	0.28953	0.0547	0.9932	0.9913
30M	0.628318	152.94	0.34168	0.0625	0.9890	0.9867
40M	0.837758	124.35	0.37772	0.0689	0.9842	0.9815
50M	1.047197	107.17	0.40533	0.0743	0.9791	0.9759
60M	1.256637	95.736	0.42779	0.0790	0.9738	0.9701
70M	1.466076	87.583	0.44681	0.0832	0.9682	0.9641
80M	1.675516	81.476	0.46333	0.0869	0.9625	0.9580
90M	1.884955	76.728	0.47821	0.0903	0.9567	0.9518
100M	2.094395	72.929	0.49122	0.0934	0.9508	0.9455
200M	4.188790	55.716	0.58229	0.1143	0.8916	0.8832
300M	6.283185	49.821	0.64141	0.1260	0.8373	0.8269
400M	8.377580	46.787	0.68806	0.1335	0.7898	0.7782
500M	10.471970	44.915	0.72843	0.1387	0.7485	0.7363

Table 3.1: Numeric values of attenuation factors for surface-wave term.

3.2.1 Path loss as a function of frequency:

Considering Intra-Body Communication applications, it is crucial to understand how the electric field decreases from the transmitter (TX) to the receiver (RX). Therefore the path loss is defined as the relationship between the two electric fields $E_{ZRX}(r, k)$ and $E_{ZTX}(r_0, k)$. In particular, the absolute value of this ratio will be analyzed as a function of the distance of the RX r and the wavenumber k

$$\left| \frac{E_{ZRX}(r, k)}{E_{ZTX}(r_0, k)} \right| = \left| \frac{k(1 - u^2 + u^4 F(r, k) \cdot \frac{1}{r}) + 1 \cdot \frac{1}{r^2} - \frac{1}{k} \cdot \frac{1}{r^3}}{k(1 - u^2 + u^4 F(r_0, k) \cdot \frac{1}{r_0}) + 1 \cdot \frac{1}{r_0^2} - \frac{1}{k} \cdot \frac{1}{r_0^3}} \right| \quad (3.22)$$

Where r_0 refers to the TX reference distance, determined by the size of the signal electrode.

Figures 3.2 and 3.3 show the module of the transfer function in a frequency range from 100 kHz to 1 GHz, well beyond the frequencies used in IBC applications, for different distances between TX and RX, using the values obtained from table 3.1 [30]. As it can be seen, the factor $1/r^3$ is dominant for low frequencies, so, since the quasi-static term is inversely proportional to the frequency, at low frequencies the modulus of the transfer function is very small. On the contrary, the term $1/r$ is dominant at high frequencies, so considering that the quasi-static term is negligible and that the surface-wave term is proportional to the frequency, the magnitude of the transfer function increases as the frequency increases. The behavior of the modulus of the ratio, which appears in equation 3.22, is like a high-pass filter [30]. In conclusion, the modulus of the frequency response can be approximated as follows

$$\left| \frac{E_{ZRX}(r, k)}{E_{ZTX}(r_0, k)} \right| = \begin{cases} \left| \frac{r_0^3}{r^3} \right|, & \text{at a low frequency} \\ \left| \frac{F(r, k) \cdot r_0}{F(r_0, k) \cdot r} \right|, & \text{at a high frequency} \end{cases} \quad (3.23)$$

If r_0/r is very small, by increasing the frequency, the modulus of the transfer function increases and a high pass filter is obtained, as already discussed. However, if the distance between TX and RX r increases, at high frequencies, the attenuation factor F decreases; therefore, the transfer function reaches a peak and then decreases rapidly, influenced by the distance. As mentioned, at greater distances, the surface-wave term is dominant and this is proportional to F , which, however, decreasing with distance, causes a lower value of the transfer function at high frequencies and greater distances. In this case, the quasi-static approach can no longer be considered; and the graph of figure 3.3 shows a band-pass behavior because the cut-off frequency decreases.

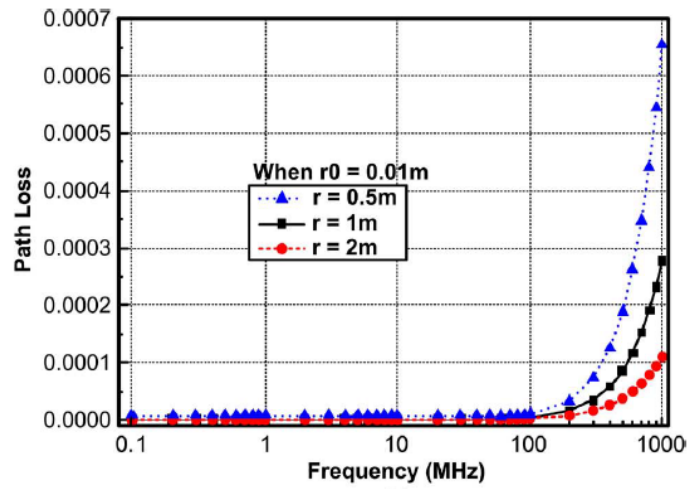


Figure 3.2: Path loss as a function of frequency for a distance $r = 0.001$ m from the TX.

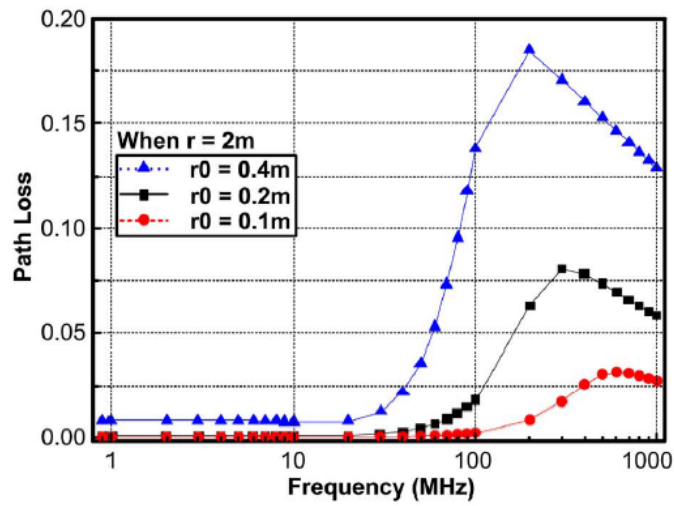


Figure 3.3: Path loss as a function of frequency for a distance $r = 2$ m from the TX.

3.2.2 Path loss as a function of distance:

Moreover, the path loss also depends on the distance between the transmitter and the receiver signal electrode. In this case, the transfer function module can be simplified as

$$\left| \frac{E_{ZRX}(r, k)}{E_{ZTX}(r_0, k)} \right| = \begin{cases} \left| \frac{\frac{1}{k} \cdot \frac{1}{r^3}}{E_{ZTX}(r_0, k)} \right|, & \text{at a short distance} \\ \left| \frac{k(1-u^2+u^4)F(r, k) \cdot \frac{1}{r}}{E_{ZTX}(r_0, k)} \right|, & \text{at a long distance} \end{cases} \quad (3.24)$$

The path loss as a function of distance can be observed in figure 3.4. It is obtained for distances that go from $r_0 = 0.1$ m and it can be noted that the decreased modulus of the transfer function is more evident for higher frequencies.

An exponential trend is observed as a function of the distance of the RX from the TX. In fact, for small distances, the quasi-static coupling is dominant. In particular, k is a function of the frequency. It is inversely proportional to the frequency used, hence at higher frequencies (300 MHz in figure 3.4), the value of k decreases by increasing the value of the path loss, while for lower values of frequency, the permittivity increases, decreasing the modulus of the transfer function.

Similarly, for longer distances, the surface-wave term is dominant. The attenuation factor is no longer considered constant and decreases as the distance r increases, reducing the path loss. This behavior is evident at higher frequencies since F is also frequency-dependent. In particular, it decreases as the frequency increases [30].

Moreover, the transfer function module for a frequency equal to 300 MHz is shown in logarithmic scale in figure 3.4. The slope of the curve in the logarithmic scale is practically constant. Therefore it can be concluded that the path loss decreases exponentially with the distance between transmitter and receiver.

In figure 3.5 the behavior of all the terms contributing to the electric field at the RX site (quasi-static coupling term, reactive-radiation term, surface-wave term) is shown as a percentage of the total value (given by the sum of all these three terms) for a signal emitted by the transmitter at a frequency of 50 MHz. It can be seen that at shorter distances, the quasi-static term is dominant, with a contribution exceeding the 50 % for distances just below 1 m. The induction field (reactive-radiation term) and the quasi-static field are about equal, and the surface-wave term increases, becoming the most relevant term as the distance increases.

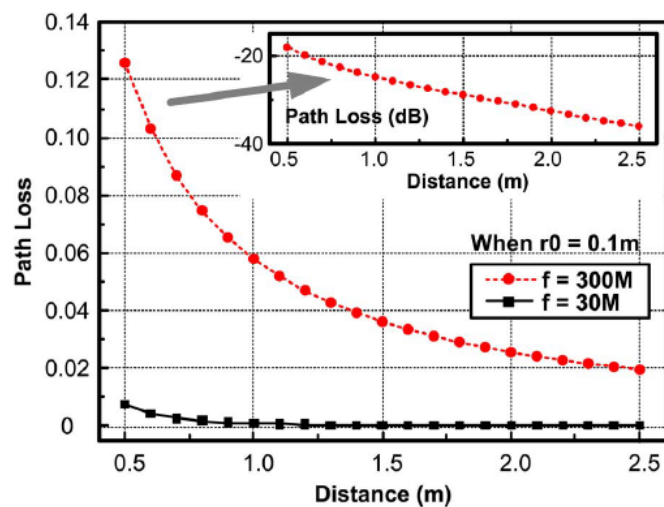


Figure 3.4: Path loss as a function of distance from the TX for two different frequencies: 300 MΩ and 30 MΩ. It is also shown the logarithmic path loss, measured as $20\log(\text{pathloss})$.

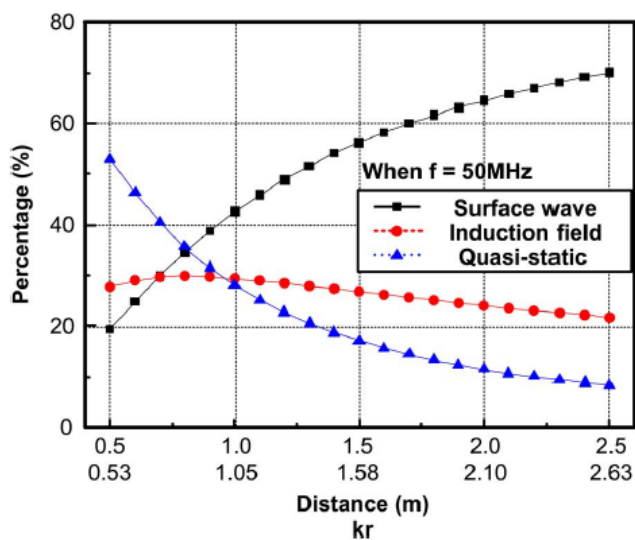


Figure 3.5: Surface-wave, Induction-field and quasi-static field contributions to the total electric field at the receiver node as functions of distance and distance multiplied by the wave number. The plot refers to a 50 MHz wave emitted by the transmitter.

Chapter 4

Live Wire

4.1 Overview

Live Wire is a device initially designed by Crepaldi et al. [5] which uses capacitive coupling to allow visually impaired subjects to recognize metal objects and interact with them. It consists of a transmitter (TX), directly powered by the power grid, connected to metal objects through a signal electrode that brings the entire surface of the object to the same potential. The user, wearing a second device, the receiver (RX), powered by batteries, allows the electric field to propagate through the body, touching the metal surface and closing the circuit to ground thanks to the effect of a parasitic capacitance that couples the receiver to ground.

Since the TX is directly connected to ground, the SNR (signal-to-noise ratio) is kept constant regardless of the RX position on the user body. At the same time, a high impedance pick-up is obtained. The signal is generated at the TX level by a GPIO (General Purpose Input/Output) pin used for PWM (pulse width modulation), allowing the analog output signal of the DAC (digital-to-analog converter) to be modulated in frequency, generating a square wave. Considering the frequencies used in the literature for IBC applications, Crepaldi [5] chose a 3.3 V peak-to-peak square wave, zero offset, frequency of 550 kHz and duty cycle of 50 %.

The RX front-end has been implemented to amplify the signal and demodulate it, thus allowing to read and recognize the differences due to the touch by the user, which in the previous application were tens of mV [32].

In this version of the device, the most significant difference is represented by a new microcontroller. It was decided to replace the STM32L486RG with the STM32F722. In table 4.1 the main characteristics of the two microcontrollers are shown.

	<i>STM32L486RG</i>	<i>STM32F722</i>
<i>Power supply (V)</i>	1.71 - 3.6	1.7 - 3.6
<i>Program flash</i>	1 Mbytes	512 kbytes
<i>SRAM</i>	128 kbytes	256 kbytes
<i>Number of I/Os</i>	114	140
<i>ADC</i>	3x12 bit	3x12 bit
<i>DAC</i>	2x12 bit	2x12 bit

Table 4.1: Key properties of STM32L486RG and STM32F722: power supply range, flash memory and SRAM memory dimension, number of I/Os, number of DACs and ADCs.

The STM32F722 was used integrated into a *Pyboard D-series with STM32F722 and WiFi/BT*. It provides different tools which can be used for different applications. "*Pyboard D-series is a compact low power module which runs microPython*" [33]. This miniaturized module can be used as a standalone device and an embedded board to accomplish its scopes.

There is a 40-40 bus connector on the back side of the board, whose pin give the possibility to communicate with the microcontroller and all the other features. The USB connectivity allows the user to program it easily with a serial prompt and a flash drive. The microPython module also includes a micro-USB connector, allowing serial communication and also the possibility to power the microcontroller.

Among all the hardware features of the microPython board, the WiFi and Bluetooth modules (4.1) have been the most used because they allow the user to enable communication with a PC displaying all the results during the device training test. It includes an on-board chip antenna, a micro SD card slot, 46 independent General Purpose Input/Output pin and other 11 GPIOs shared with other modules. These GPIOs are available through 24 holes along the board and the 40-40 WBUS connector. In our application, this bus connector has been used to connect the main microPython board to a WBUS-DIP 28, the *MicroPython board D adapter with power management IC* [37]. It allows the communication to 24 GPIOs and

gives the user another possibility to power the board through an external battery leading the alimentation to the Pyboard (PYBD) microcontroller. On the back side of this secondary board, a 20 pin bus connector to plug-in a temperature sensor, the TILE-SENSA, another essential feature to improve the quality and quantity of the information exchange between the TX and the RX, hence allowing the user to improve his knowledge about the object status.

Because of the possibility of powering the Pyboard through an external battery, the WBUS-DIP 28 also includes a battery charger that is suitable only for Li-ion batteries exploiting the USB FS port. In this application, a Pyboard D-series with STM32F722 and WiFi/BT and a WBUS-DIP 28 have been installed on both receiver and transceiver devices to allow a complete bidirectional communication flow and to give them the possibility to switch from TX to RX and vice versa. It may represent a necessary improvement for some possible future applications, as will be discussed.

In figure 4.1 a top and bottom view of the PYBD with all its integrated modules is shown.

There are several possibilities to power the Pyboard even if, as already dis-

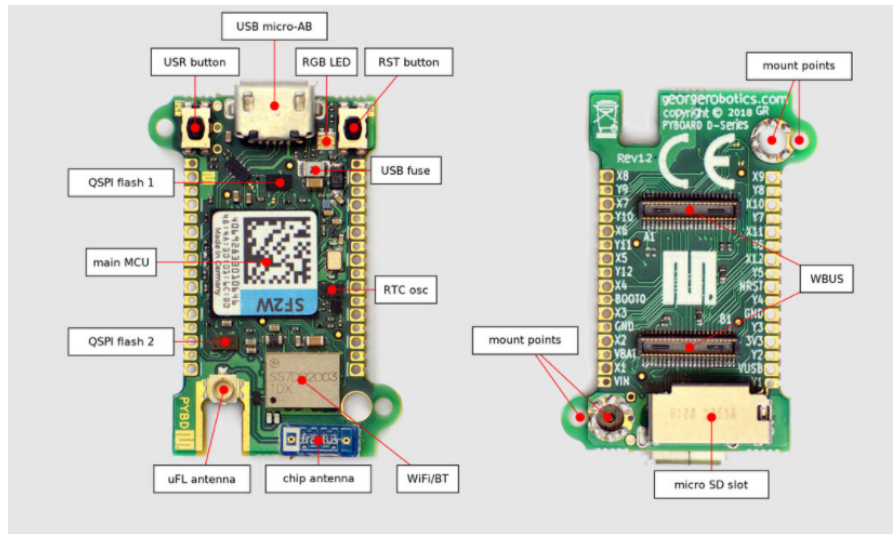


Figure 4.1: Top and bottom view of the microPython board.

cussed, the TX is directly powered by the power grid and the RX by a Li-ion battery. For instance, a USB cable via its port on the Pyboard can be used, as well as the VUSB pin. In this case, the voltage has to be in the range of 4.8 V

- 5.2 V. Finally, the VIN pin can be used. For this power supply method, the voltage has to be between 3.2 V and 4.8 V. These different solutions represent a significant advantage during the device training test.

4.2 Design architecture and performed functions

The device counts three different boards, the PYBD and the WBUS-DIP 28, have already been discussed. The third one has to be connected to the WBUS-DIP 28. In this way, it can be linked to the Pyboard microcontroller. This last board has been designed on *Altium Designer*. by Crepaldi et al. [5], but in this work, several features have been replaced, improved, or removed. The TX and RX architecture will be discussed in the next sections, starting from their schematics and justifying all the design choices made.

4.2.1 Transceiver design and schematic

In figure 4.2 the TX schematic is shown. The X6 signal is taken from the PYBD microcontroller DAC and it is placed at the input of an OP-AMP (U8A in figure 4.2), the LT1804CS8, used as voltage follower as it was observed that without using a buffer, the pin of the DAC could not provide the current required by the circuit. The output of the OP-AMP, powered between 0 and 3.3 V, goes to the ADG713BRZ (U6 in figure) input, it is a switch used to realize the square wave transmitted by the TX. The ADG713BRZ is a monolithic CMOS device containing four independently selectable switches [34]. Only the first switch is used in this application, controlled by the Y6 signal, taken from a microcontroller GPIO. It is used for PWM; in particular, it changes its state every microsecond to have the signal at the output of the integrated circuit first switch when it is at a high logic level. In this way, a square wave at the frequency of 500 kHz is obtained at the non-inverting input pin of a second OP-AMP (U8B in figure), also used as a voltage follower to decouple the switch output signal from the rest of the circuit.

When the user capacitively closes the circuit towards ground, by touching the signal electrode, it allows the current to pass through the circuit, in particular through the sensing resistor R15/R16/R17, causing a potential drop which will be amplified and filtered to recognize the touch.

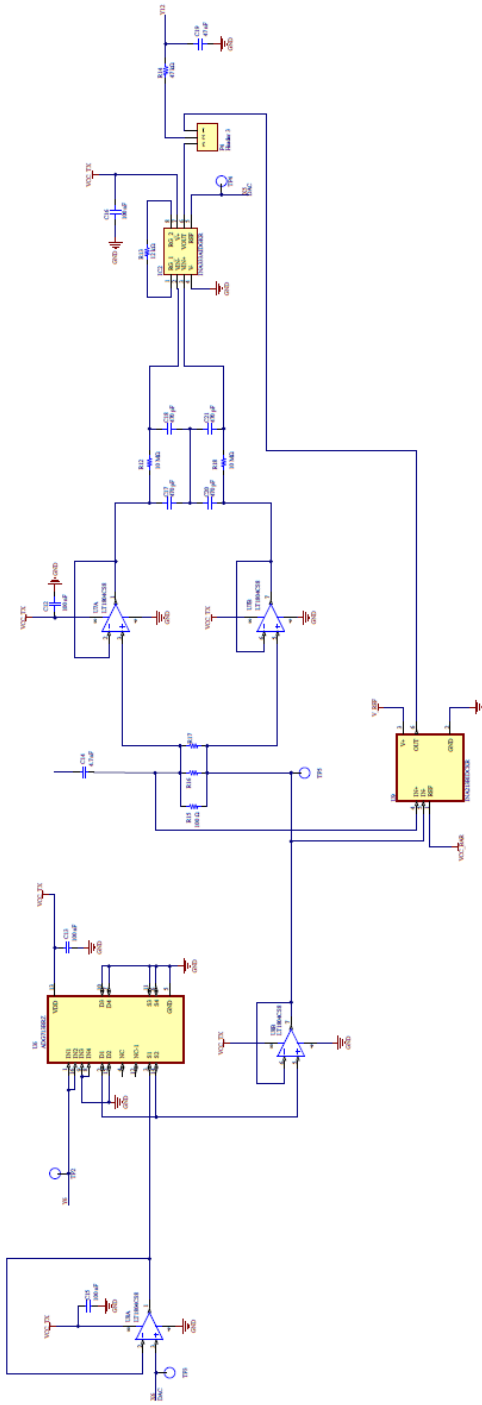


Figure 4.2: Schematic of the TX module.

In theory, when the user is not touching the electrode, the signal at the U8B output will be the same on both sides of the sensing resistor (R_s). While when the circuit closes capacitively, a small current will flow over R_s causing a potential drop that has to be recognized. However, in the open-circuit condition, the voltage drop over the sensing resistor is never equal to zero. This is due to parasitic phenomena; after R_s and C14, there is a parasitic capacitance that couples the transmitter to ground and introducing a low-pass RC filter. This represents a problem as a low-pass filtered square wave has components that will be attenuated at frequencies higher than the filter cut-off frequency, equal to $f_c = \frac{1}{2\pi RC}$. Thus, the two different signals over R_s will then be amplified, compromising the touch-detection module specificity.

Touch detection is carried out separately by two different circuits. The presence of two instrumentation amplifiers characterizes each one. Crepaldi [5] used an INA333, IC2 on the schematic, to amplify the signal over the sensing resistor in a differential way. The INA333 is an instrumentation amplifier with gain adjustable via an external resistor, R13, which allows the signal to be amplified differentially at its inputs by applying an offset imposed by the REF pin. In the previous version of the *Live Wire*, Paone [32] used a dual power supply to power the TX, between -3.6 V and 3.6 V, setting a null reference for the INA333. Here it was decided to use a single 3.3 V supply voltage and the reference signal for the INA333 was set at half dynamic, 1.65 V, thanks to the use of the microcontroller DAC through the X5 pin. The gain of the instrumentation amplifier is

$$G = 1 + \frac{100k\Omega}{R_G}$$

A resistor R_G of 12 k Ω was used to obtain an overall gain of about 9.3 [35]. Before the amplifier, two OP-AMPs, U7A and U7B, respectively, were used to decouple the two signals over the resistor R_s . Then they will be filtered by a low-pass filter, with cut-off frequency $f_c = 48$ Hz in order to reduce the high-frequency noise.

Besides, it was also decided to use another instrumentation amplifier, to offer an alternative to the INA333. The INA213 is an instrumentation amplifier with a fixed gain equal to 50 that offers excellent performance, especially for current/voltage sensing [36]. Its gain is so high that it is advantageous, especially for those applications where wide dynamic ranges are required. In this case, a 3.3 V power supply increases the risk of saturating the integrated circuit, mostly if parasitic phenomena that couple the circuit to ground occur. However, considering that

the application consists of recognizing the touch by the user, we are not directly interested in preventing the amplifier saturation but in recognizing the two different voltage levels that correspond to touch and non-touch conditions. Therefore, the problem occurs only if the amplifier saturates in an open circuit, so when no one is closing the circuit by touching the signal electrode. If it were already in saturation due to parasitic capacitance, it would not go out of saturation in user touch condition, compromising the effectiveness of touch detection.

Finally, after the INA333, a RC low-pass filter is placed, with $R_{14} = 47 \text{ k}\Omega$ and $C_{19} = 47 \text{ nF}$, consequently the frequency of the pole is $f_c = \frac{1}{2\pi R_{14} C_{19}} = 72 \text{ Hz}$.

To solve the problem regarding the amplifier saturation, it can be either reduced the R_s resistance value or the C_{14} capacitance. As the resistance or capacitance decreases, the frequency of the pole f_c increases, reducing the attenuation at higher frequencies and the difference between the two signals across the resistor R_s in open circuit condition.

Figure 4.3 shows the low-pass behavior of the RC circuit. C_p is a parasitic capacitance which couples the signal electrode to ground; the equivalent capacitance given by the series of C_{14} and C_p is equal to

$$C_{eq} = \frac{C_{14} \cdot C_p}{C_{14} + C_p}$$

Then the frequency of the pole is

$$f_c = \frac{1}{2\pi R_s C_{eq}}$$

Alternatively, the amplitude of the square wave generated by the DAC could also be decreased. In fact, by reducing the signal amplitude, the drop over the resistor decreases as well, bypassing the problem linked to the choice of R_s and C_{14} . This possibility will be discussed later, when the results of the touch detection will be presented, varying the resistance of R_s and the output value of the DAC.

However, when the circuit is closed, it has to be considered that by decreasing the value of R_s , the voltage drop across the sensing resistor will also decrease, making the touch detection more difficult for the ADC. Using a 500 kHz wave, the receiver input stage impedance is about $1 \text{ M}\Omega$ and the expression of the tension over the sensing resistor can be approximated as directly proportional with R_s because it goes from $1 \text{ }\Omega$ to $100 \text{ }\Omega$ so it is negligible compared to the high impedance path to ground:

$$V_s = V_{in} \frac{R_s}{R_s + R_{in}}$$

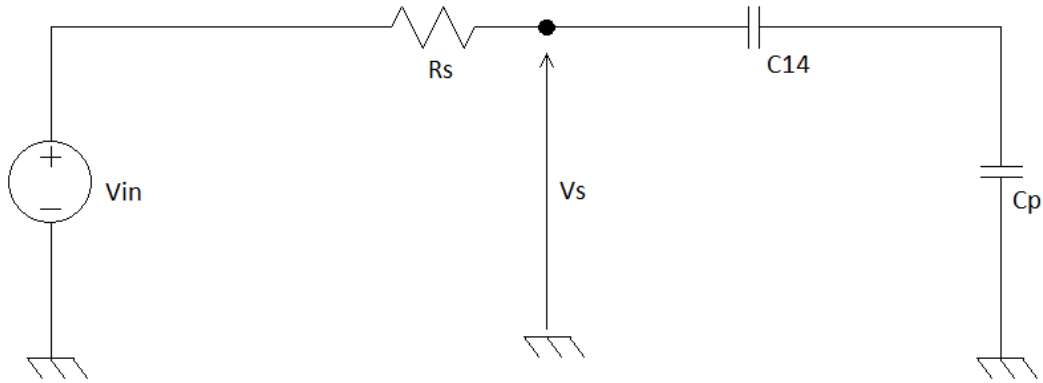


Figure 4.3: Electric model of the open circuit at the TX stage, parasitically coupled to ground. It represents a low-pass filter causing a voltage drop over R_s .

Where V_s is the voltage after the sensing resistor, V_{in} is the signal before the sensing resistor and R_{in} is the receiver input stage impedance at 500 kHz. Since $R_s + R_{in} \approx R_{in}$, then $\frac{R_s}{R_s + R_{in}} \approx \frac{R_s}{R_{in}}$ and $V_{in} - V_s \approx V_{in} \frac{R_s}{R_{in}}$.

As regards the open circuit condition, for the INA333, it was observed that, whatever the value of R_s in the range 1Ω - 100Ω and for any amplitude of the square wave, a capacitor with a capacitance value equal to 4.7 nF , does not cause the saturation of the amplifier, characterized by a gain fixed by the resistor $R_{13} = 12 \text{ k}\Omega$. The INA213 is characterized by a higher gain, equal to 50. It goes into saturation in open circuit condition for any value of R_s in the range from 1Ω to 100Ω , using a square wave amplitude of 3.3 V . Therefore it was decided to replace the capacitor C_{14} with another capacitor with a smaller capacitance, suitable for both instrumentation amplifiers. It has been observed that a capacitance equal to $1/10$ of the previous one avoids the saturation of the integrated circuit. Hence it was decided to use a capacitor $C = 470 \text{ pF}$. In this way, the cut-off frequency of the low-pass filter has been increased, preventing the amplifier from going into saturation and keeping R_s constant, thus not decreasing the performance of the touch detection. To evaluate the new performances of the INA213 and to know for which wave amplitudes and resistance values it goes into saturation, using the 470 pF capacitor, tests with ten different DAC output signals and nine different

resistance values have been performed. Table 4.2 shows the results of the tests carried out.

R (Ω) \backslash Amplitude (V)	3.30	3.11	2.90	2.70	2.48	2.28	2.07	1.66	1.24	0.83
1	O	O	O	O	O	O	O	O	O	O
2	O	O	O	O	O	O	O	O	O	O
3	O	O	O	O	O	O	O	O	O	O
5.1	O	O	O	O	O	O	O	O	O	O
10	O	O	O	O	O	O	O	O	O	O
20	X	O	O	O	O	O	O	O	O	O
30	X	X	X	O	O	O	O	O	O	O
51	X	X	X	O	O	O	O	O	O	O
100	X	X	X	O	O	O	O	O	O	O

Table 4.2: Saturation occurrence, changing R_s and the signal amplitude. 'O' represents missing saturation, 'X' represents the presence of saturation in open circuit condition.

INA213 goes into saturation in open circuit condition, for the highest signal amplitudes and R_s . These results can be explained by considering that higher values of the two parameters correspond to a higher voltage drop over the sensing resistor even when the user is not touching the object to which the TX is connected, as previously discussed. In particular, it is noted that for values that cause saturation of the amplifier, the voltage value obtained is approximately zero because the INA213 saturates towards lower voltages, considering the current flow direction and the pin order of the instrumentation amplifier.

For high values of R_s and output of the DAC, a more sensitive and effective touch detection system is obtained. Consequently, the best value for the sensing resistor and square wave amplitude have to be found in the lowest-left area of table 4.2. The most significant tests already described in the table are shown below.

Tests carried out consist of one minute of acquisition divided into blocks of 10 seconds. For the first 10 seconds, the user does not touch the signal electrode. In the next 10 seconds, the touch takes place. This cycle is repeated three times.

Figure 4.4 shows signals during the 60 s acquisitions, changing R_s value. As it can be noted, the square wave amplitude of 830 mV is too low to appreciate signal differences for all the sensing resistor values, which during measurements assumed values indicated from table 4.2. In figure 4.5 the square wave mean value decreases as R_s increases. However, any difference can be observed over time because of the low sensitivity of the system using an amplitude of 2.07 V. In figure 4.6, with a

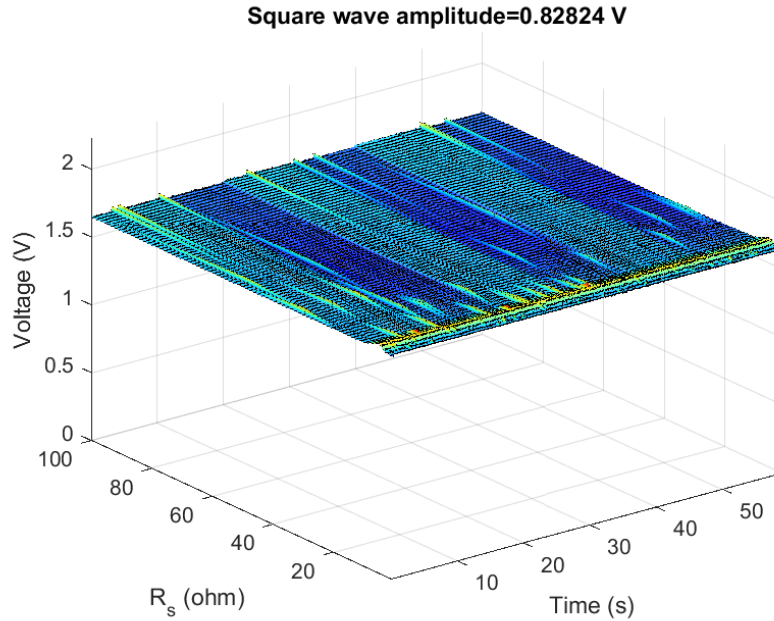


Figure 4.4: Signal over sensing resistor during acquisition, varying R_s , for an amplitude of the square wave of 0.83 V.

square wave amplitude of 2.70 V, differences can be observed only for the highest values of R_s . For the lowest ones, signal mean value increases because of the higher value of the low-pass filter cut-off frequency due to the parasitic capacitance. Finally, in figures, 4.7 and 4.8 the highest amplitude values, 2.90 V and 3.3 V, cause saturation for the highest values of resistance and a very high sensitivity to touch detection for the lowest ones.

Figure 4.9 represents the same acquisitions discussed previously, in which the sensing resistor value is fixed, while the signal amplitude changes according to table 4.2. As it can be seen, the square wave profile is shown only for the highest amplitudes, while for the lowest ones, it can not be observed any changes during the acquisition. Figures 4.10 and 4.11 represent the same result, but it has to be highlighted the decreased mean value of the voltage drop over R_s , for each signal amplitude. In particular, for $R_s = 10 \Omega$, it can be observed the highest voltage drop, between the touch and non-touch condition, for the highest value of square wave amplitude. Finally, in figures 4.12 and 4.13 saturation occurs at the highest

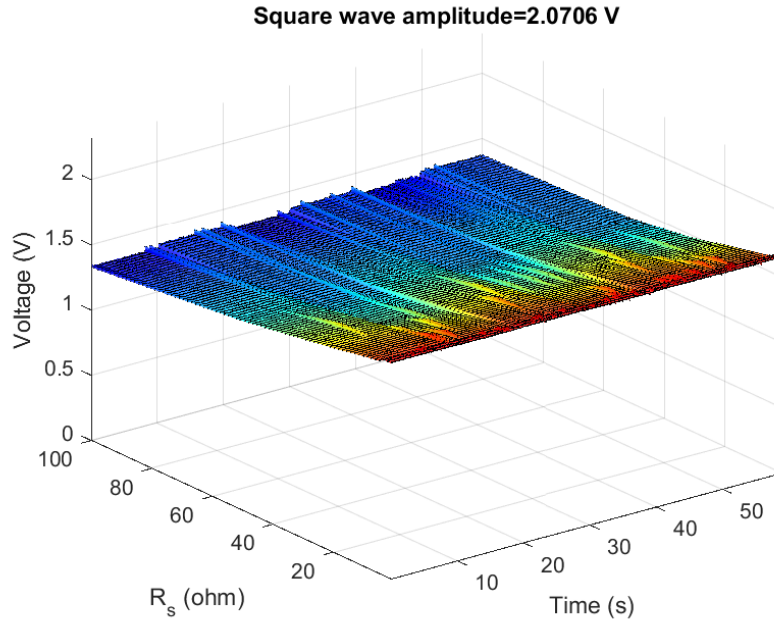


Figure 4.5: Signal over sensing resistor during acquisition, varying R_s , for an amplitude of the square wave of 2.07 V.

signal amplitudes, as confirmed in table 4.2; moreover, the touch detection sensitivity is decreased as well.

In particular:

- Figure 4.14 shows that for lowest R_s and DAC output, the ADC input signal does not allow to recognize the touch. Only noise can be recognized during acquisitions using $R_s = 1 \Omega$ and square wave amplitude equal to 830 mV. The average value of the open circuit signal, i.e., at the beginning of the acquisition, is very similar to the reference voltage set for the INA213, 1.65 V. In fact, with a low resistance value of R_s and signal amplitude, the drop voltage over the resistor is very close to zero (even in case of touch the same level is observed, because the system is not sensitive enough).
- Figure 4.15 shows better results than the previous ones. There are much more significant variations between touch and non-touch signals. These differences are about 40 mV, obtained using $R_s = 51 \Omega$ and signal amplitude of 2.48 V. The signal average, while the user was not touching the electrode, is about

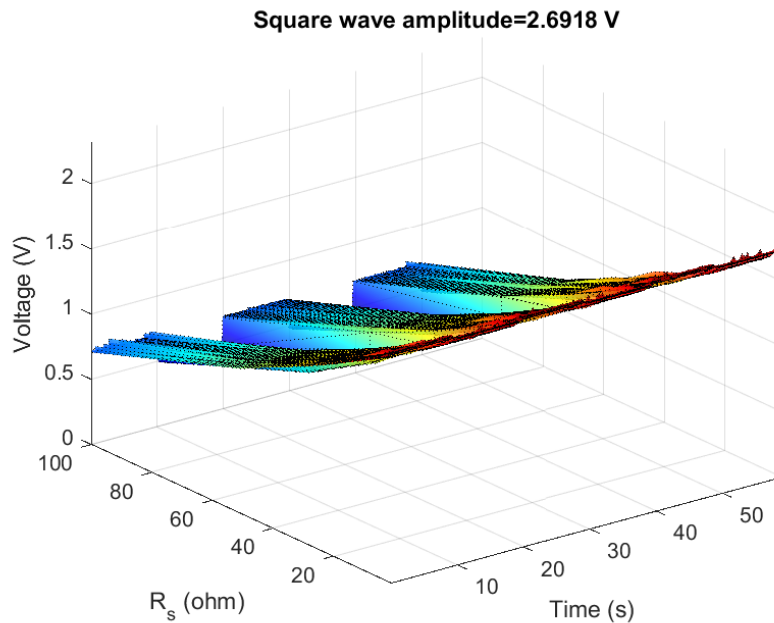


Figure 4.6: Signal over sensing resistor during acquisition, varying R_s , for an amplitude of the square wave of 2.70 V.

1.39 V. This value, lower than in the previous case, shows that a higher drop voltage over R_s in open circuit condition is present. It is due to both the higher amplitude of the wave imposed by the DAC and the reduced cut-off frequency of the low-pass circuit caused by the higher resistance value.

- Figure 4.16 shows the configuration which obtained the best results. In this case, $R_s = 10 \Omega$ and signal amplitude of 3.3 V. Variations between the touch and the non-touch conditions are about 800 mV. In contrast, the average value of the open circuit signal is about 1 V, even less than the other cases.
- Figure 4.17 finally, shows that with a $R_s = 100 \Omega$ and signal amplitude of 3.3 V, the INA213 goes into saturation and it is not possible to recognize touch in any way by the user. The average value of the signal is about zero, demonstrating the integrated saturation is a condition that occurs in all configurations marked with an 'X' in table 4.2.

Signals in figure 4.15 and 4.16 show that the difference in the case of touch condition is large enough to be recognized by the analog-to-digital converter of the

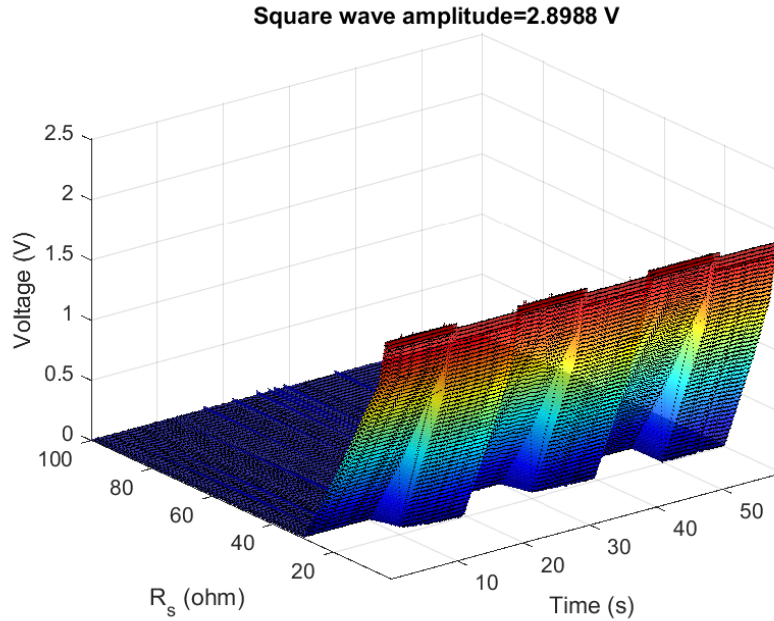


Figure 4.7: Signal over sensing resistor during acquisition, varying R_s , for an amplitude of the square wave of 2.90 V.

PYBD. In fact it is a 12-bit ADC, with 3.3 V input dynamics, so its resolution is

$$ris = \frac{D_{A/D}}{2^{N_{bit}}} = 806 \mu V$$

Figure 4.18 shows the signal obtained with a square wave amplitude of 2.48 V and $R_s = 51 \Omega$ filtered with a moving average filter ($N_{samples} = 10$). The difference between the two levels is about 40 mV, much lower than those for signals obtained with other configurations but still about 50 times greater than the ADC resolution. Figure 4.19 shows the same results obtained with an amplitude of 3.3 V and $R_s = 10 \Omega$. In particular, a variation of about 800 mV is observed, which is about 1000 times greater than the ADC resolution. Figures show that the touch can be easily recognized using the INA213. In fact, in the lower part of the figure, it is reported how events are correctly classified.

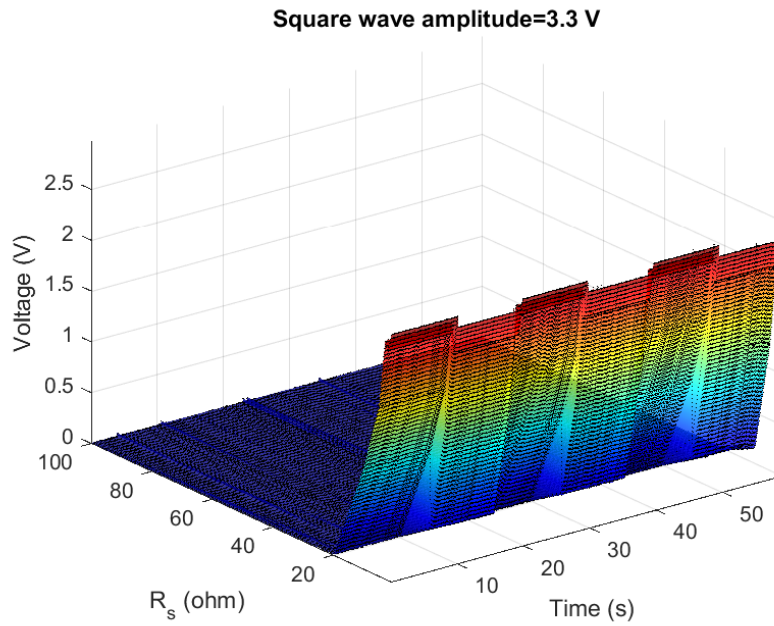


Figure 4.8: Signal over sensing resistor during acquisition, varying R_s , for an amplitude of the square wave of 3.3 V.

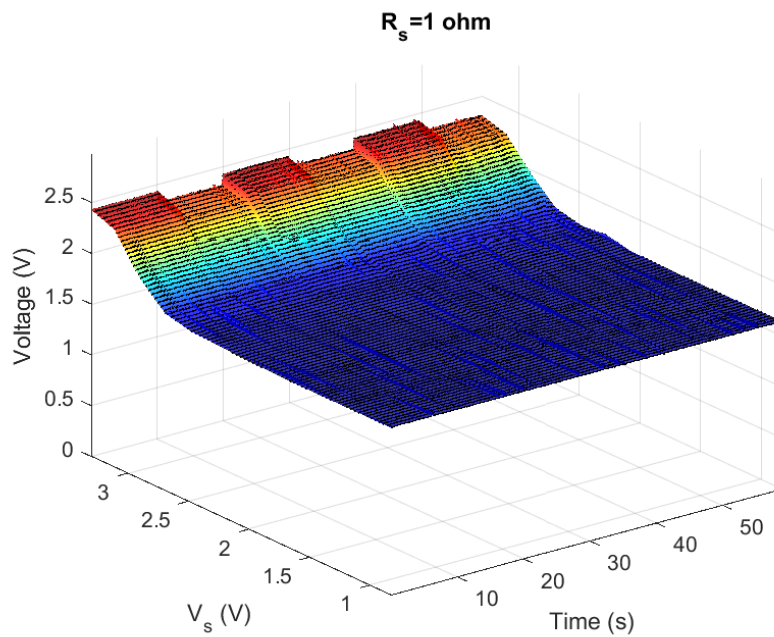


Figure 4.9: Signal over sensing resistor during acquisition, varying the signal amplitude, for $R_s = 1 \Omega$.

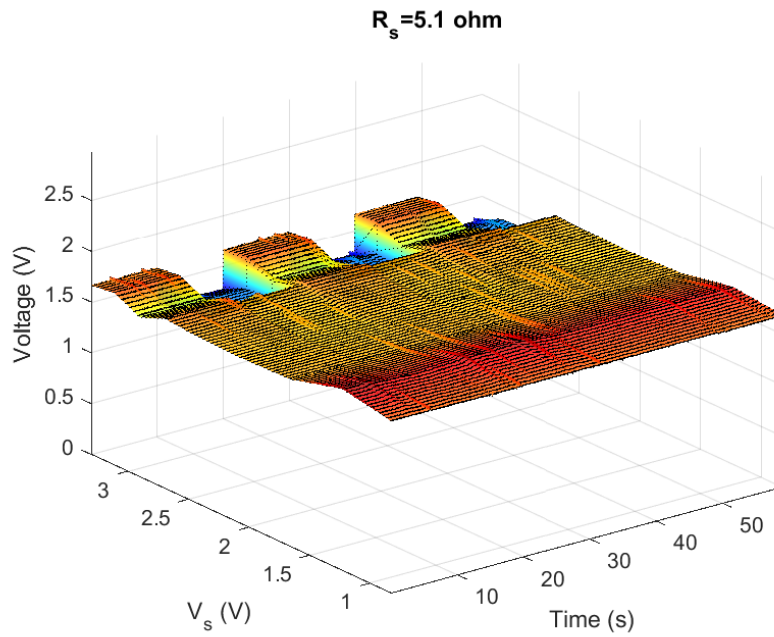


Figure 4.10: Signal over sensing resistor during acquisition, varying the signal amplitude, for $R_s = 5.1 \Omega$.

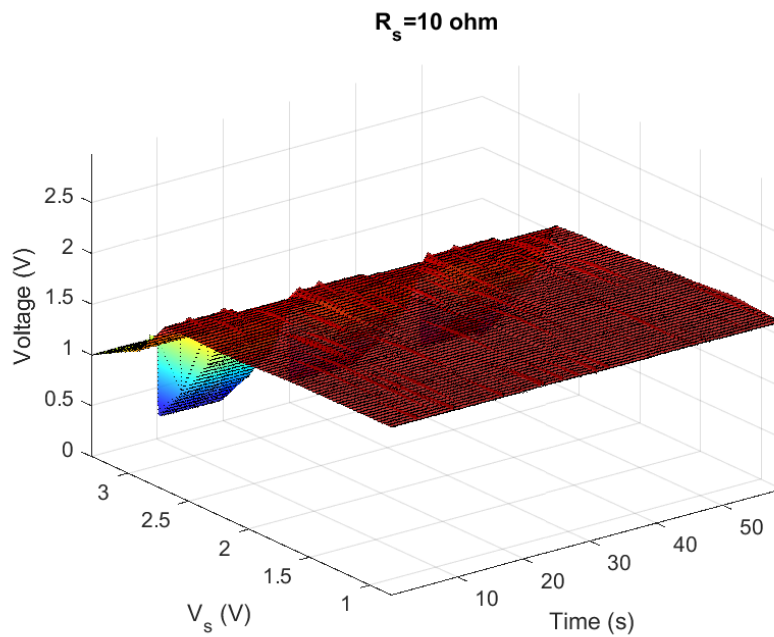


Figure 4.11: Signal over sensing resistor during acquisition, varying the signal amplitude, for $R_s = 10 \Omega$.

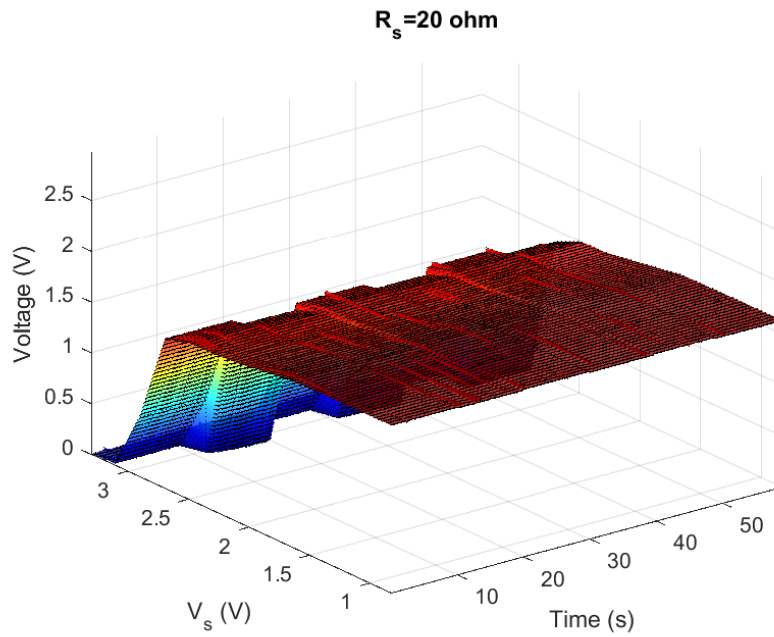


Figure 4.12: Signal over sensing resistor during acquisition, varying the signal amplitude, for $R_s = 20 \Omega$.

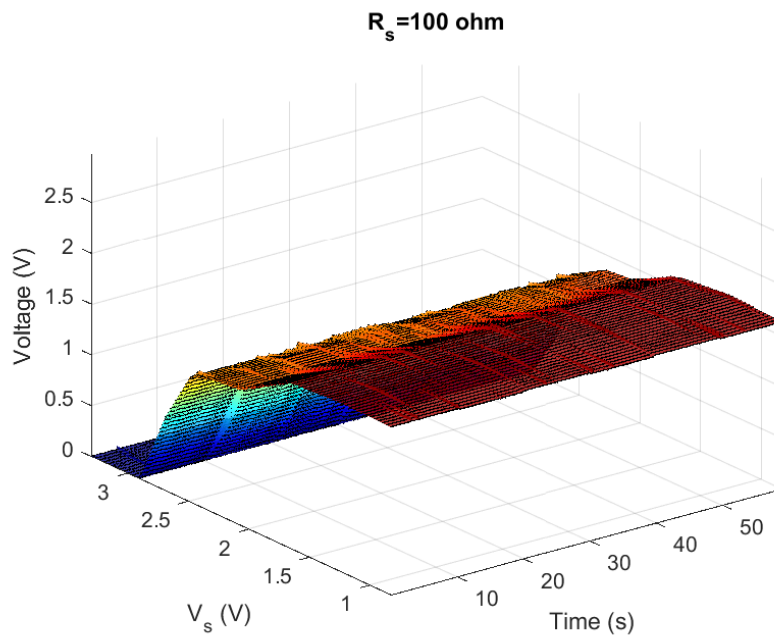


Figure 4.13: Signal over sensing resistor during acquisition, varying the signal amplitude, for $R_s = 100 \Omega$.

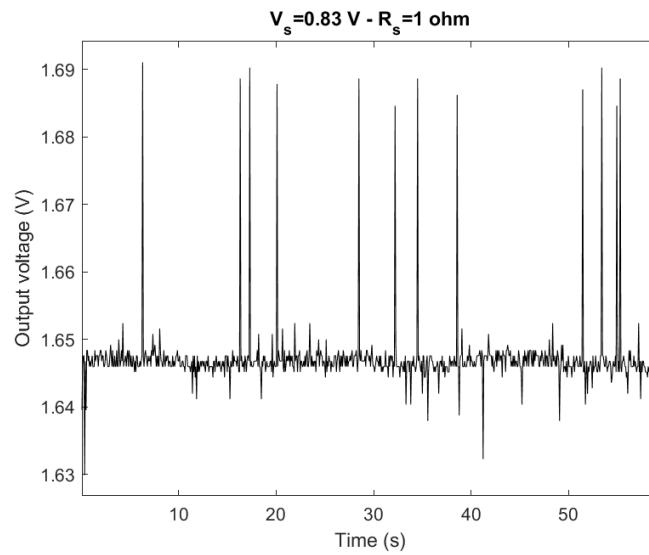


Figure 4.14: Acquisition showing the ADC input signal, performed with the INA213. From 0 to 10 s, the user is not touching. From 10 s to 20 s he is touching the signal electrode. the cycle is repeated until 60 s are reached. $R_s = 1 \Omega$ and signal amplitude of 830 mV.

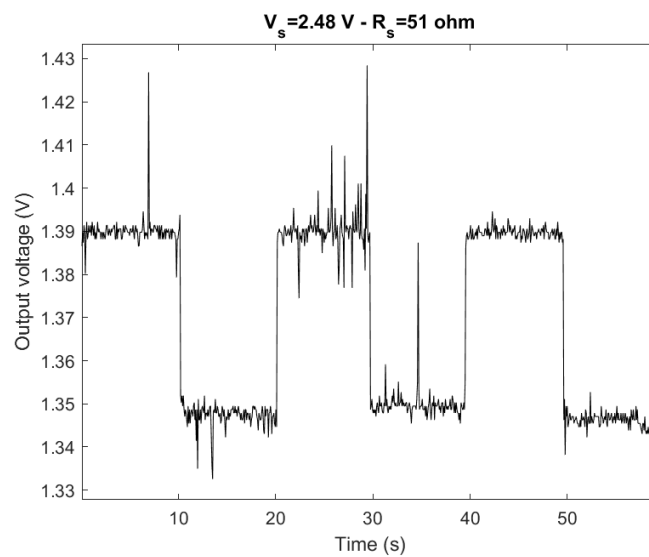


Figure 4.15: Acquisition showing the ADC input signal, performed with the INA213. From 0 to 10 s, the user is not touching. From 10 s to 20 s he is touching the signal electrode. the cycle is repeated until 60 s are reached. $R_s = 1 \Omega$ and signal amplitude of 2.48 V.

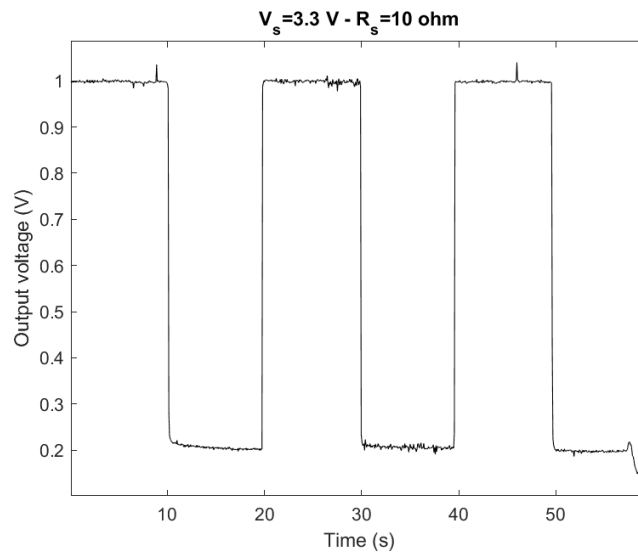


Figure 4.16: Acquisition showing the ADC input signal, performed with the INA213. From 0 to 10 s, the user is not touching. From 10 s to 20 s he is touching the signal electrode. the cycle is repeated until 60 s are reached. $R_s = 1 \Omega$ and signal amplitude of 3.3 V.

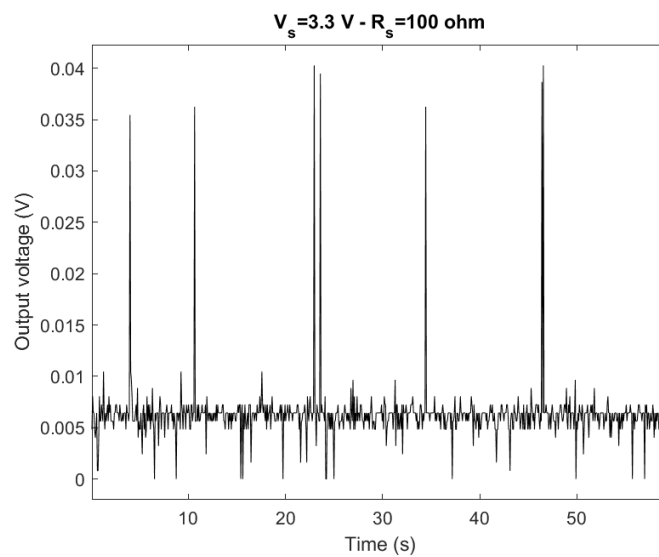


Figure 4.17: Acquisition showing the ADC input signal, performed with the INA213. From 0 to 10 s, the user is not touching. From 10 s to 20 s he is touching the signal electrode. the cycle is repeated until 60 s are reached. $R_s = 1 \Omega$ and signal amplitude of 3.3 V.

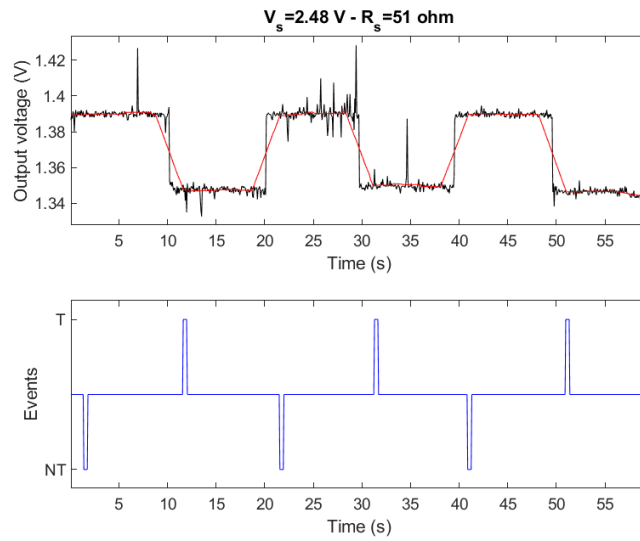


Figure 4.18: Touch detection signal with $R_s = 51 \Omega$ and signal amplitude of 2.48 V. The signal filtered by a moving average ($N = 10$) is superimposed, in red. The touch detection algorithm result is shown in the second plot.

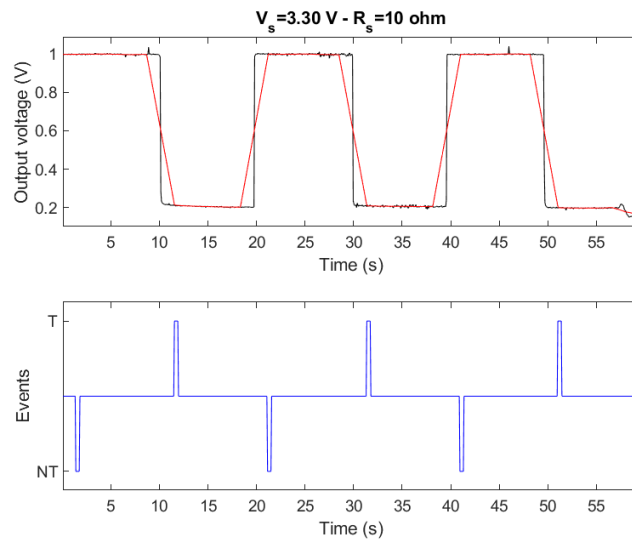


Figure 4.19: Touch detection signal with $R_s = 10 \Omega$ and signal amplitude of 3.30 V. The signal filtered by a moving average ($N = 10$) is superimposed, in red. The touch detection algorithm result is shown in the second plot.

4.2.2 Receiver design and schematic

The receiver has a less complex structure than the transmitter. Figure 4.20 shows its schematic. At the front-end input, there is a high-pass RC filter. C25 performs the same function as C28 for the TX; it cuts the DC component. R26 is a 26 k Ω resistor that implies a cut-off frequency of approximately 4.8 kHz, given the capacitance value of C25 equal to 33 pF. The square wave generated at the filtered TX level passes through an OP-AMP; it has to amplify the signal increasing its dynamics of a value equal to VCC_BAR. This voltage value is taken from the REF1933AIDDCT, which will be treated in the next section, and is equal to half the power supply. Before being read at the input of the microcontroller ADC, the signal goes to the input of a precision rectifier, a circuit element consisting of an operational amplifier and one or two diodes, depending on whether it is in a standard configuration or in an alternative configuration. In this case, the rectifier allows to amplify the input signal when it is lower than VCC_BAR, the amplification is equal to $\frac{R24}{R25} = \frac{220k\Omega}{4.7k\Omega} = 46.81$. Finally, two first-order RC low-pass filters, both with a 27 k Ω resistor (R22 and R23) and capacitor of 47 pF (C22 and C23), have to remove components at higher frequency before the analog-to-digital converter reading, setting the cut-off frequency at 125.4 kHz.

As already mentioned, each device has both the TX and RX module. They

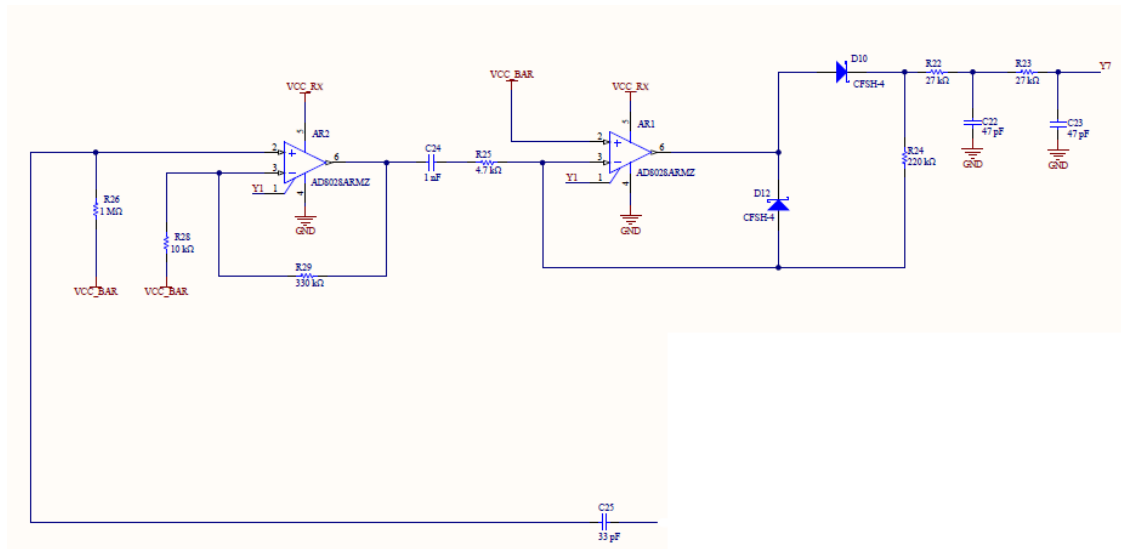


Figure 4.20: Schematic of the RX module.

have to be separated and powered by different blocks. Thus, it was decided to use two switches driven with inverted logic to avoid both being connected to the electrode. In order to perform this function, the possibilities discussed are:

- *Electronic switches:* two electronic switches can be used to select which module has to be connected to the electrode. In this case, it has to be considered that the electronic switch which links the RX to the electrode is exposed to the risk of being at very high potentials, considering that the RX is floating. It does not represent a problem because the integrated circuit can not be easily damaged, in fact it is equipped with protection circuits; but a high potential could saturate it and make it inactive for a very long time.

A possible solution is shown in figure 4.21, where sw1 and sw2 represent the two electronic switches. Moreover, C is the only capacitor used, placed after the switches and before the electrode. It consists of placing the capacitor after the switch to cut the continuous component responsible for any saturation of the integrated. In this way, we can use the electronic switches, but we would be forced to choose the same capacitor for both the TX and the RX, which could represent a problem in the test phase, where it is essential to be able to try different capacitance values, in order to maximize device performances.

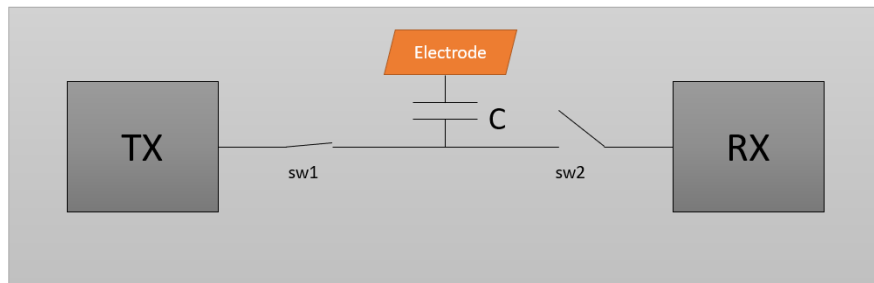


Figure 4.21: Schematic blocks representing the link between the TX/RX and the signal electrode using two electronic switches sw1 and sw2 and one capacitor C.

- *Relè:* on the other hand, two relè can be used instead of the electronic switches. In this way, we could keep two different capacitors, one for the receiver and one for the transmitter. This second possibility is shown in figure 4.22, where the two mechanical switches are indicated by r1 and r2, while

the two different capacitors by C1 and C2.

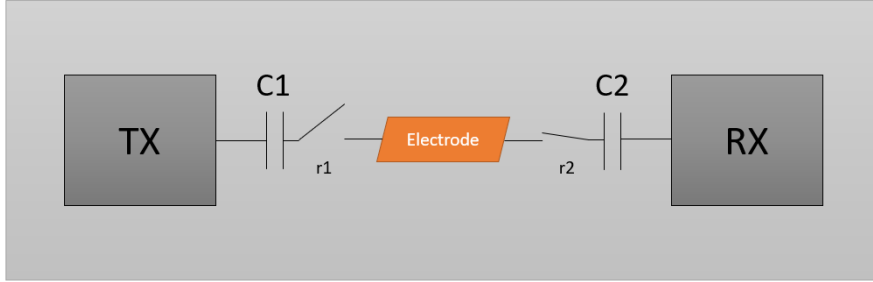


Figure 4.22: Schematic blocks representing the link between the TX/RX and the signal electrode using two relè r1 and r2 and two different capacitors C1 and C2.

Above all, the greater flexibility during tests makes the second option more suitable than the first one. Consequently, two relè were used, placed between C9 and C14, with different power supplies but driven so that they never connect both the TX and the RX to the electrode.

In addition to the touch detection, Paone [32] decided to make the device more specific. It has been developed a system to recognize if it is the RX user or someone else who is not wearing the RX to perform the touch. Thus, a bidirectional communication system between TX and RX has been developed. It exploited an impedance mismatch that, in transmission lines, caused a signal reflection, originating a different voltage drop over R_s . If it is large enough to be detected by the ADC, it allows recognizing the RX user.

Paone [32] used an electronic switch placed before the RX front-end, which switches the signal from the front-end to a pin at the potential of half the RX power supply value or directly to the RX ground, as shown in figure 4.23. In particular, the impedance mismatch occurs when it switches from the pin connected to the RX front-end to one of the others because this signal default path has a matched impedance to the TX signal electrode, its value is $Z_{FE} = 1 \text{ M}\Omega$ at 500 kHz. Therefore, by switching between these three pin, a backpropagation of the signal was obtained, which allowed the instrumentation amplifier to identify one of the following three conditions:

- *No touch is occurring*

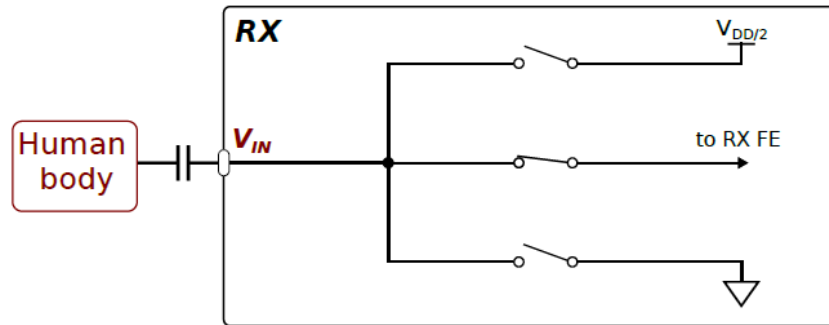


Figure 4.23: Previous *Live Wire* RX user recognition system. A difference in the path to ground impedance is exploited, switching between three pin: the first one at half power supply potential ($V_{DD}/2$), the second linked to the RF front-end and the third one directly to ground.

- *The RX user is touching the signal electrode*
- *Someone else without wearing the receiver is touching the electrode*

In this work, we first tried to use the RX relè, which, by switching, would change the impedance of the circuit, causing a signal difference to recognize the presence of the RX user. In particular, it was decided to switch the relè, CRR03-1AS, at a frequency of 1 Hz so that the circuit was connected to the RX front-end for 500 ms and remained floating for other 500 ms. The CRR03-1AS is a SPST switch. Therefore there was no possibility of closing the circuit to ground when not connected to the front-end. The impedance difference between the front-end and the capacitive path to ground, when RX is floating, should ensure the presence of different enough current levels to allow the ADC to recognize two distinct voltage values.

However, significant differences were not observed, so we tried to use a relè that allowed to connect the circuit to the front-end or directly to ground through a low impedance path, therefore using a relè SPDT. Also in this case, it was not obtained any positive result, as the ADC did not show any significant variation of the signal at the relè switching frequency.

Subsequently, it was also tried to increase the coupling of the receiver to ground, the same ground to which the SPDT relè connects the circuit. The configuration used is shown in figure 4.24.

The RX has been placed within a black case on the right forearm and two

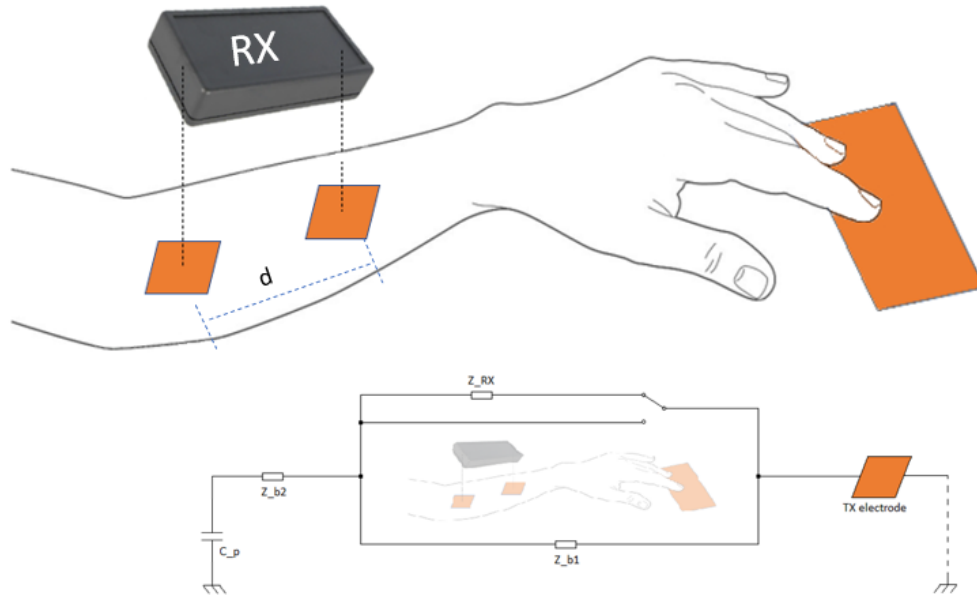


Figure 4.24: Representation of the RX electrodes directly in contact with the skin. The first one represents the RX signal electrode while the second one allows to increase the ground coupling, by coupling the receiver to the human body. The electric model is reported below.

different electrodes are directly in contact with the skin. The first one takes the TX signal from the human body while touching the signal electrode. The second one is connected to the RX ground. Because of the contact with the skin, it will minimize the path to ground impedance by reducing the parasitic capacitance. By reducing the effects of parasitic phenomena, an attempt was made to maximize the current through the RX circuit at a frequency of 1 Hz, increasing the system sensitivity. Furthermore, it can be observed from the electrical model in the figure that as the distance d between the two electrodes increases, the impedance value Z_{b1} increases as well. The partition ratio is modified, favoring the current flow through the other branch, through the relè and the RX front-end circuit. In particular, by keeping the two electrodes on the same arm, the difference in signal amplitude can not be recognized by the ADC. A significant increase in the signal has been noted, placing the second electrode in contact with the other forearm.

The signal difference can be easily recognized by the ADC, as shown in figure 4.25. The acquisition has been performed with a Rigol MSO5104 digital oscilloscope on the input pin of the TX ADC.

Although results are quite encouraging, this solution is very uncomfortable, as

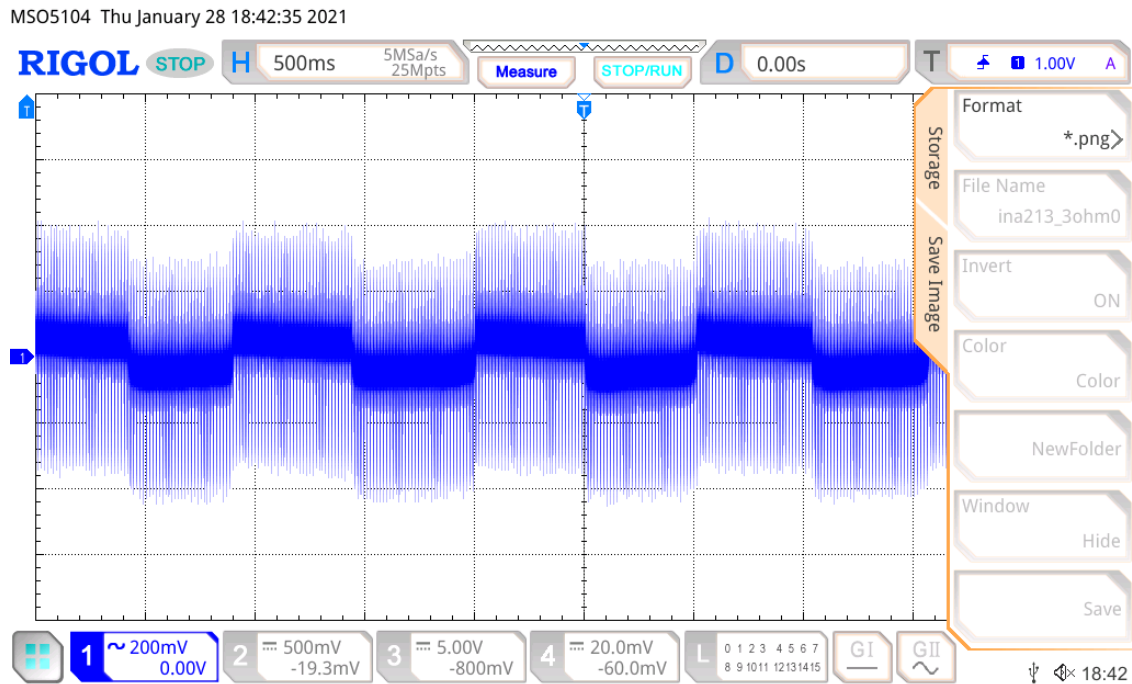


Figure 4.25: TX ADC signal acquisition while the RX relè switches between ground and RX front-end at 1 Hz. The RX electrode was placed on the right forearm while the right hand was touching the TX signal electrode. The RX ground electrode was placed on the left forearm, increasing the distance "d" as much as possible.

the two electrodes connected to the receiver must be at a considerable distance between them. Therefore it is impractical for the RX user.

Finally, it was decided to increase the switching frequency between the front-end and ground. In fact, in this way, the impedance of the parasitic capacitance that closes the circuit to ground may be reduced, allowing the passage of a higher current and consequently increasing the system sensitivity. The use of a relè is inconvenient, as it cannot reach switching frequencies large enough to significantly reduce the parasitic capacitance that couples the RX to ground. An electronic switch has to be used again but to do this, the configuration in figure 4.22 is no

longer usable. In conclusion, the final structure of the device is that indicated in figure 4.21 where only one capacitor is used, for the reasons already explained, positioned between the electrode and the electronic switch that connects it to the TX or RX. At the same time, the other will be left floating. The capacitance value used for the capacitor is equal to 470 pF, i.e., the value of C14 in figure 4.2, as it has been observed that it also guarantees the correct operation of the receiver. Moreover, that value allows to solve the problem of parasitic coupling to ground of the TX signal electrode, as already discussed.

The electronic switch used closes the circuit towards ground for 200 ms, then switches every 1 μ s between 3.3 V and ground for others 200 ms. In this way, the parasitic capacitance has a much lower impedance, given by using a signal at a frequency of 1 MHz, which becomes higher when the switch remains in conduction to the ground for other 200 ms. Therefore a signal difference significant enough to be recognized by the ADC should be obtained. Indeed, figure 4.26 shows an acquisition made by the transmitter analog-to-digital converter. It can be observed that at the frequency of 5 Hz, every 200 ms, there are significant differences between the two levels.

However, it must be considered that results shown in figure refer to a perfectly conductive contact, using a conductive wire, between transmitter and receiver. It has not been possible to obtain any positive result by touching the TX electrode while wearing the RX, showing that this feature is not yet ready to be implemented.

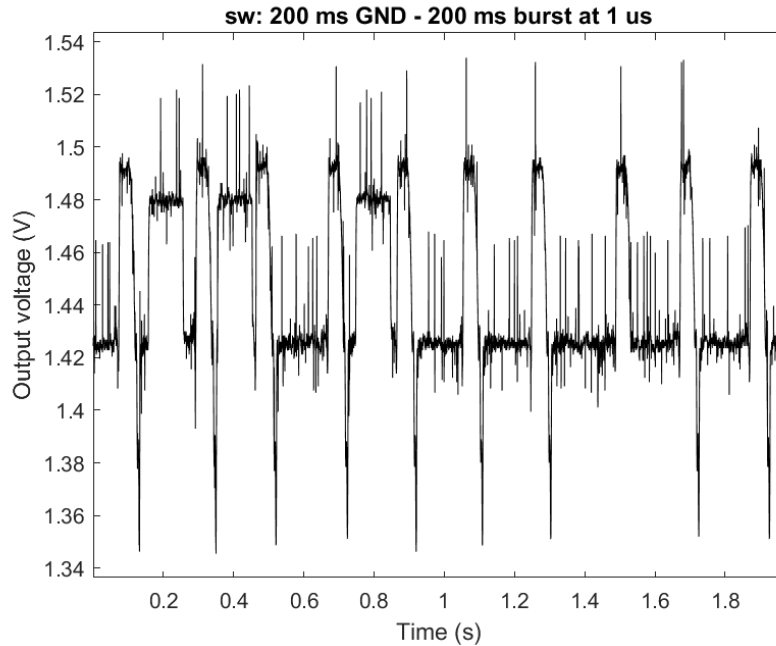


Figure 4.26: TX ADC signal acquisition while the circuit is swithing at 5 Hz between: ground and RX front-end - ground pulses at 1 MHz, for 200 ms.

4.2.3 Power supply and connection to the PYBD

While the power grid directly powers the transceiver, the receiver has to be powered by batteries. Moreover, it must be floating because it has to close the circuit to ground through a parasitic capacitance. Li-ion batteries with a no-load nominal voltage value of 3.6 V and a capacity of 750 mAh are used to accomplish this scope. WBUS-DIP 28 has a battery charging module, the BQ2407, which allows the user to recharge RX batteries via USB FS port when necessary [37], so batteries are directly connected to these pin. The power supply provided by batteries, brought at the VIN pin of the WBUS-DIP 28, powers the PYDB which uses the VIN pin to generate a stable output voltage at 3.3 V, used to power all integrated circuits of the board. It is represented by the 3V3 pin.

In table 4.3 a summary of all power ports is shown [37]. As mentioned, for both TX and RX, the power supply is brought to the VIN pin and then the stable output is taken from the 3V3 pin of the PYBD. Thus, only the third and the last

line solutions are exploited in this application.

Therefore, using the 3V3 output pin from the PYBD, it is possible to power all

Port	Use	Voltage	Notes
USB conn	power and comms	5 V	connect to PC or USB power brick
VUSB	power in	4.8 V - 5.2 V	1 A fast/0.22 Ω fuse and protective diode
VIN	power in	3.2 V - 4.2 V	also on WBUS
VBAT	backup battery	1.65 V - 3.6 V	also on WBUS
3V3	output only	3.3 V	user switchable LDO max 300 mA total

Table 4.3: Summary of the power ports provided by PYBD.

different board modules. In figure 4.27 all the power supplies for each module are shown.

Considering that the RX and the TX are integrated within the same board, when the first is powered, the second must be shut down and vice versa. Hence it is necessary to have different power supply signals to each module on the board, so having the possibility to decide which one has to be powered to reduce power consumptions. Therefore, different integrated circuits have been used; each one can enable/disable a specific power supply block of the circuit. Y9 is a PYBD GPIO pin which is used to enable/disable the TX power supply (VCC_TX) by using the TPS22860DBVR, U1 in figure, an ultra-low leakage load switch. Y10 has the same function. It has to enable/disable the RX power supply (VCC_RX) by using U3. To power the second instrumentation amplifier, the INA213, the output signal of U3 is brought to the input pin of U2, the REF1933AIDDCT. It is a low-drift, low-power, dual-output, VREF and VREF/2 voltage reference, which allows to obtain at the output pin VREF, the input signal when the enabling pin $EN \leq VIN - 0.7 V$ and at the VBIAS pin, VREF/2 [38].

Both VREF and VBIAS voltage are used to perform touch detection using the INA213, as already discussed.

Finally, Y3 and Y2 enable/disable power supply for the RX relè (VCC_Rrx) and the TX relè (VCC_Rtx).

Moreover, figure 4.28 shows all the WBUS-DIP 28 pin. They allow the board to communicate with the PYBD thanks to the connectors on the top, as shown in

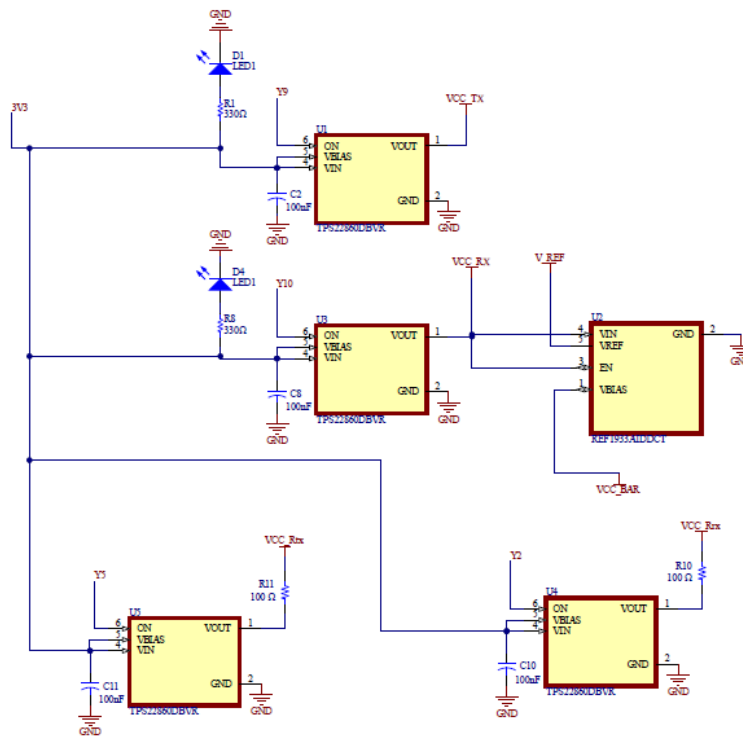


Figure 4.27: Power supply block. 3V3 pin is an output pin from the PYBD, used to obtain the power supply for the TX, the RX, the relè at TX stage, the relè at RX stage and the INA213.

figure.

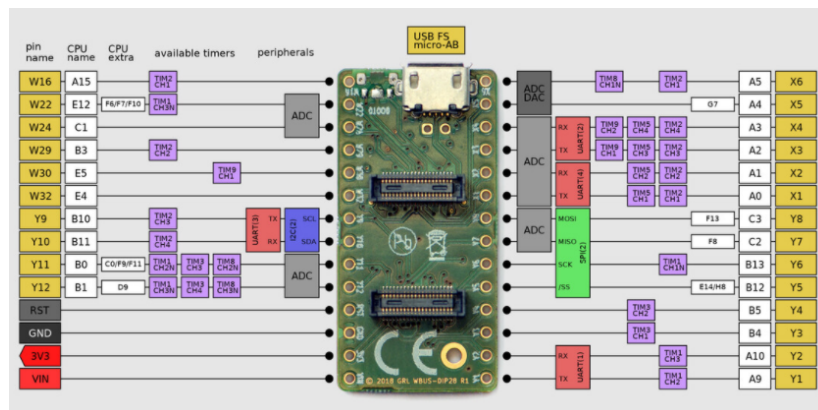


Figure 4.28: WBUS-DIP 28 board with all its input/output pin. In the center, the two bus connectors are used to plug-in the board to the PYBD.

Chapter 5

Results and Discussion

Measurements during validation acquisitions involving different persons and several objects of different sizes have been performed to confirm that the circuit can recognize the user touch and evaluate device performances. Power consumptions have been measured as well.

5.1 Touch detection

It is essential to demonstrate how the device can perform its functions in different environmental conditions, attaching the TX signal electrode to different size objects and recognizing the occurred touch performed by several persons, proving its reliability. A validation setup has been built up to accomplish this goal: 6 persons, whose data and physical characteristics are shown in table 5.1, have tested the device by verifying the touch detection algorithm on three different objects, each one characterized by a different size. In particular, a microwave oven of 45.5 cm x 30.5 cm x 27.5 cm placed on a wooden table at 86 cm from the floor, a metallic drawers of 67 cm x 45 cm x 91 cm at 13 cm from the floor and a wardrobe of 160 cm x 45 cm x 200 cm on the floor have been tested. Furthermore, eight acquisitions for each person have been obtained, each one in a different position, in order to modify as much as possible the capacitive coupling to ground: standing up, sitting down, wearing shoes, without shoes, wearing a glove, without the glove.

Acquisition protocol is the same used for INA213 tests, discussed in section 4.2.1:

	Gender	Age	Height (cm)	Weight (kg)
Subject 1	Male	24	172	80
Subject 2	Male	25	178	75
Subject 3	Female	24	164	57
Subject 4	Male	24	170	83
Subject 5	Female	25	176	67

Table 5.1: Physical characteristics of subjects involved in validation measurements.

a 60 s acquisition, in which the user touches the object every 20 s, for 10 s. 24 different data, regarding each object and configuration, have been collected and half of these, the most representative ones, are reported below. Moreover, each figure will show the same type of acquisition for each subject, thus overlapping five different graphs. The legend over each figure refers to the subject order shown in table 5.1.

The only difference from the former tests, treated in section 4.2.1, is represented by the signal amplitude generated from the microcontroller DAC at the TX level. An amplitude of 2.90 V has been preferred to 3.30 V. In this case, the electrode is connected to different size objects, involving antenna effects and increasing the current through the sensing resistor, when the subject is not touching the object, so when an open circuit occurs. All figures are filtered with a moving average, averaging over the last 20 samples. Their mean value has been removed to improve their overlapping and allowing a better data representation.

5.1.1 Microwave Oven

Results obtained for the microwave oven are the best among the objects tested; results are very stable and repeatable and all the tests carried out showed significant differences between the touch and non-touch conditions, as shown in figures 5.1, 5.2, 5.3 and 5.4. The best results were obtained when the subjects were not

wearing shoes and gloves, standing up in front of the oven, placed on a wooden table at the height of 86 cm from the floor. If shoes are not worn, the coupling to ground is maximized. If gloves are not worn, the introduction of an additional capacitance that increases the contact impedance with the object is avoided. In this configuration, a maximum difference greater than 400 mV is observed with little variability, mostly sufficient to recognize the occurred touch. Excellent results were also obtained in the other tests, never dropping below the 20 mV difference between the two levels, with an ADC resolution of $806 \mu\text{V}$, as reported in section 4.2.1. It is interesting to note how, for subjects 3 and 5, the signal is significantly lower, practically in all configurations. It may be due to their weight; in fact, a lower weight could correspond to a smaller quantity of fat, which causes a reduction in the body electrical conduction, compared to a subject with a higher percentage of fat tissue.

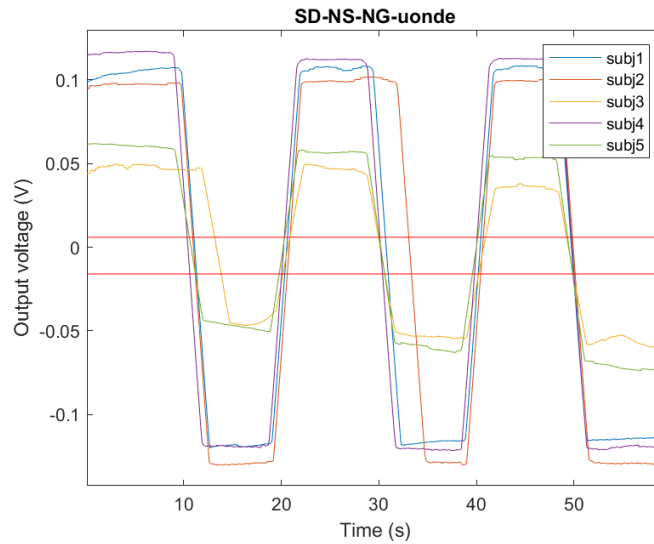


Figure 5.1: INA213 acquisition while subjects are sitting down, without shoes and without gloves, touching the microwave oven every 20 s for 10 s.

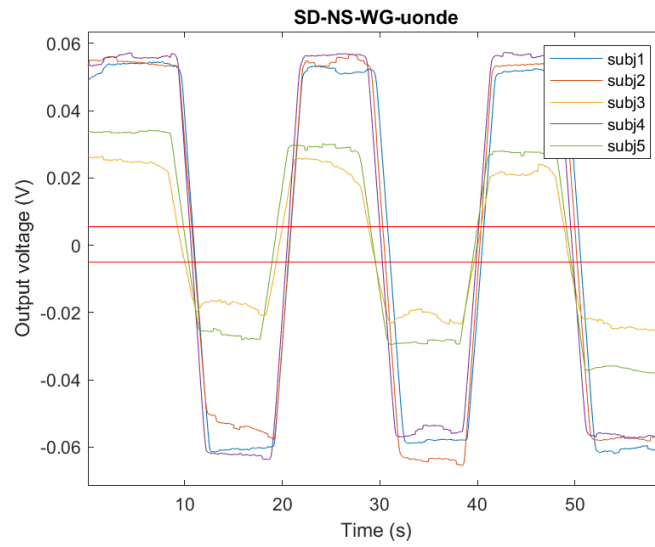


Figure 5.2: INA213 acquisition while subjects are sitting down, without shoes and with gloves, touching the microwave oven every 20 s for 10 s.

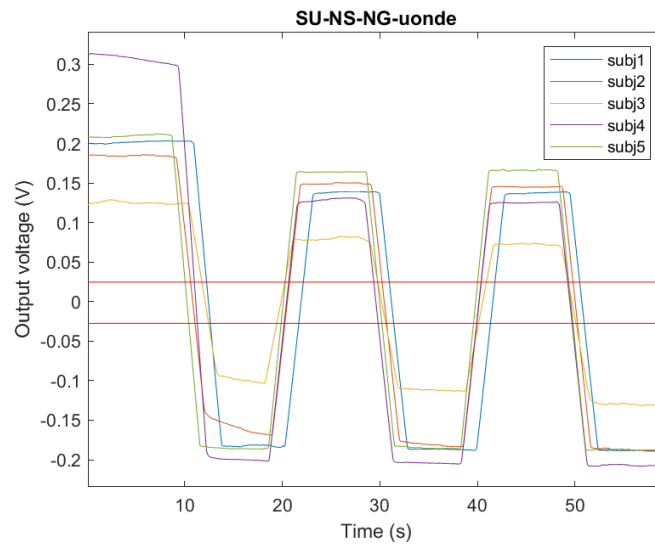


Figure 5.3: INA213 acquisition while subjects are standing up, without shoes and without gloves, touching the microwave oven every 20 s for 10 s.

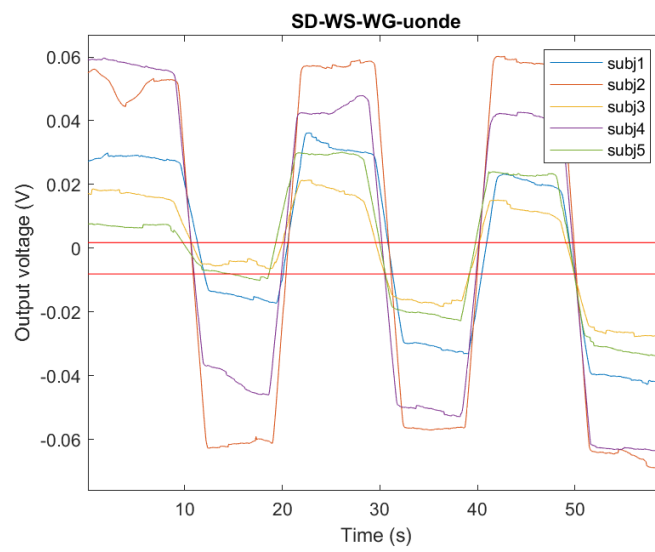


Figure 5.4: INA213 acquisition while subjects are sitting down, with shoes and with gloves, touching the microwave oven every 20 s for 10 s.

5.1.2 Wardrobe

Figures 5.5, 5.6, 5.7 and 5.8 show the acquisitions performed with the wardrobe, in four different conditions. The results obtained for the wardrobe certainly have the highest noise level; despite the moving average low-pass filter with a number of samples $N = 20$, the signal still seems to be significantly corrupted by high-frequency noise. It is certainly due to the size of the wardrobe, which acts as an antenna and causes the signal to be significantly disturbed by environmental noise. However, the ripples observed in the figure are not decisive in being able to identify the touch. Also in this case, it has been observed that a lower amplitude characterizes signals of subjects 3 and 5.

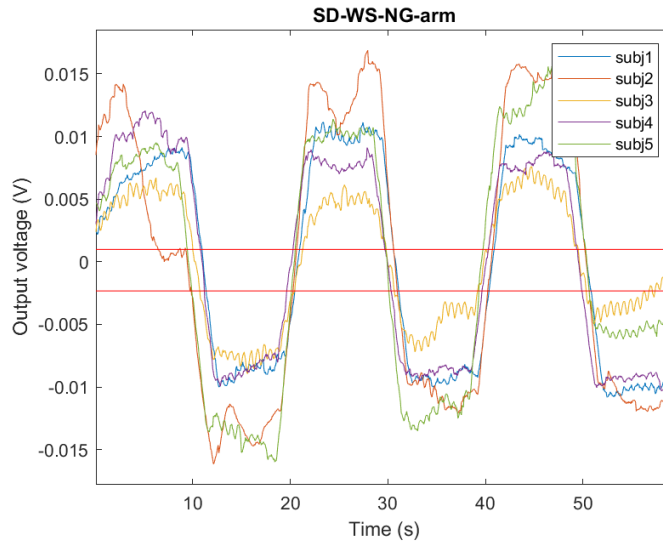


Figure 5.5: INA213 acquisition while subjects are sitting down, with shoes and without gloves, touching the wardrobe every 20 s for 10 s.

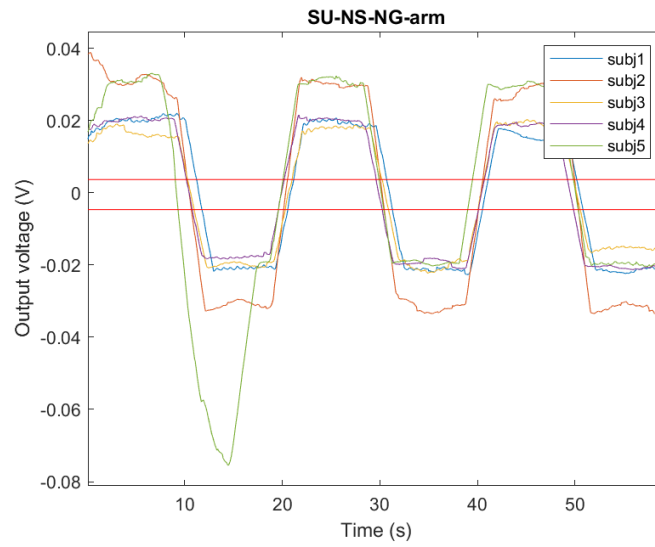


Figure 5.6: INA213 acquisition while subjects are standing up, without shoes and without gloves, touching the wardrobe every 20 s for 10 s.

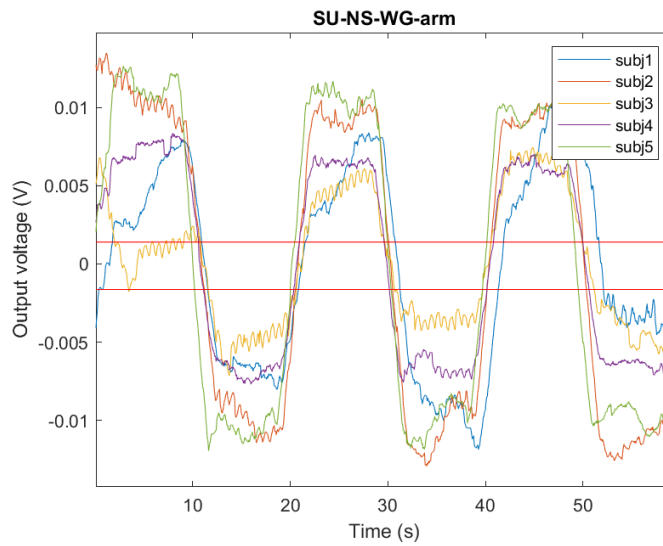


Figure 5.7: INA213 acquisition while subjects are standing up, without shoes and with gloves, touching the wardrobe every 20 s for 10 s.

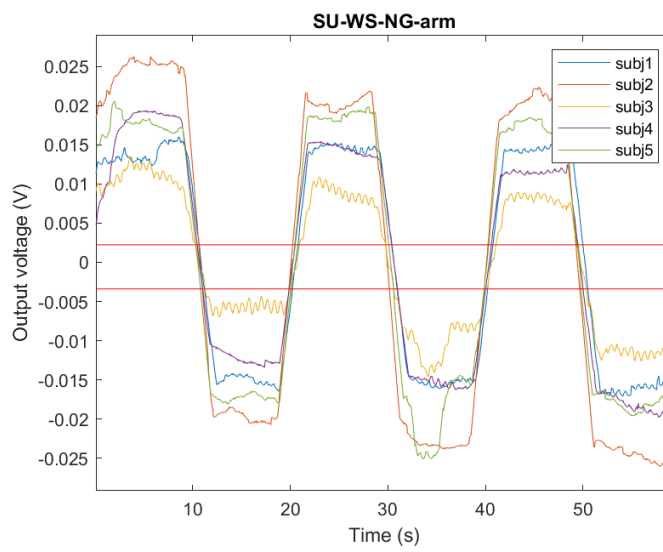


Figure 5.8: INA213 acquisition while subjects are standing up, with shoes and without gloves, touching the wardrobe every 20 s for 10 s.

5.1.3 Drawers

Also for the drawers, positive results have been observed for most configurations. When subjects are tested without gloves and shoes and standing up, the difference between the two conditions is the highest, even if slightly smaller than for the wardrobe. If the wardrobe provides the noisiest results, the drawers is characterized by more variable results than those for the other two objects. Figure 5.11 and figure 5.12 show that, especially during the first phase of the acquisition, the signal is extremely variable. It could be caused by the charge accumulated by the drawers between two tests and by the difficulty of discharging towards ground. In fact, the most significant differences are recorded in the first 10 s, after which the acquisition becomes more stable. Despite this, the transitions due to the subject touch are distinguished, regardless of the previously recorded value, so it is possible to perform touch detection.

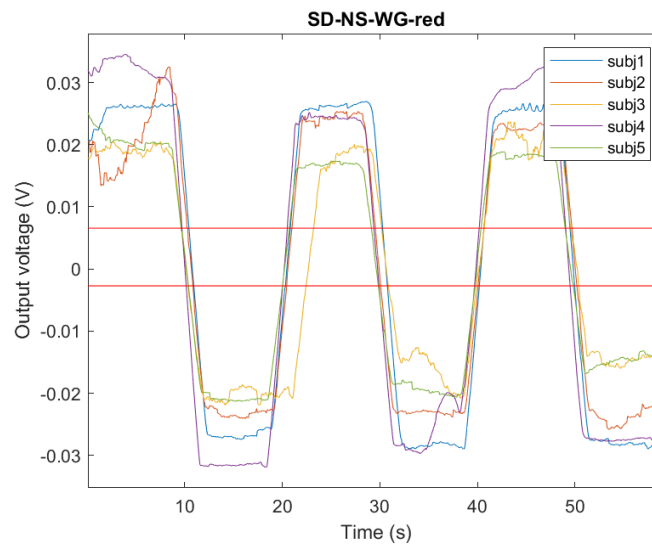


Figure 5.9: INA213 acquisition while subjects are sitting down, without shoes and with gloves, touching the drawers every 20 s for 10 s.

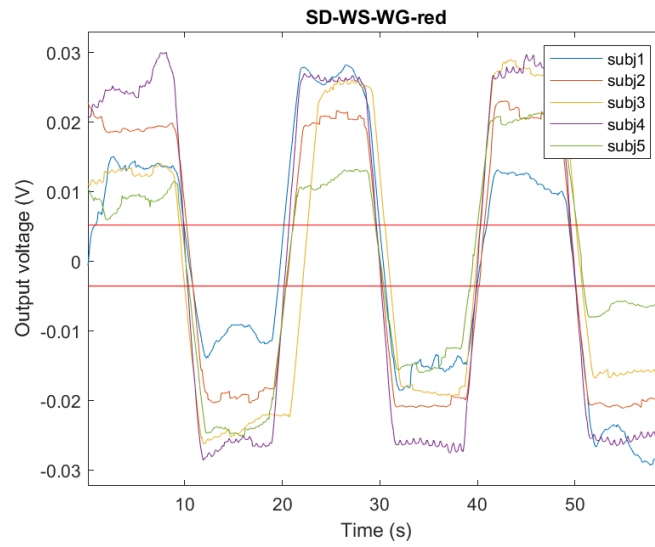


Figure 5.10: INA213 acquisition while subjects are sitting down, with shoes and with gloves, touching the drawers every 20 s for 10 s.

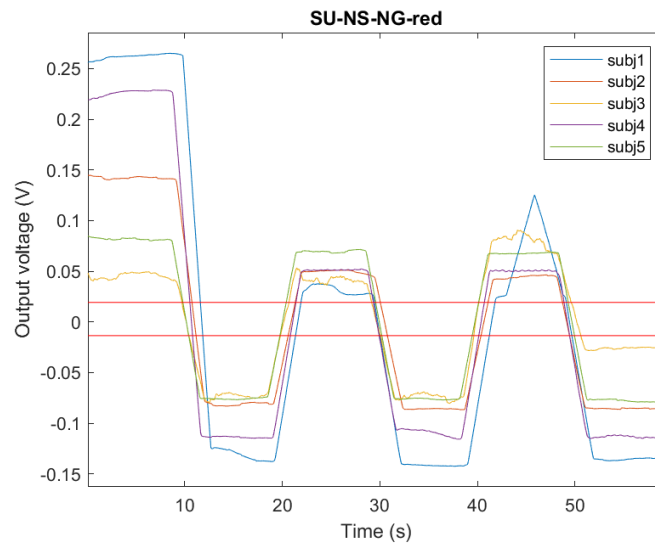


Figure 5.11: INA213 acquisition while subjects are standing up, without shoes and without gloves, touching the drawers every 20 s for 10 s.

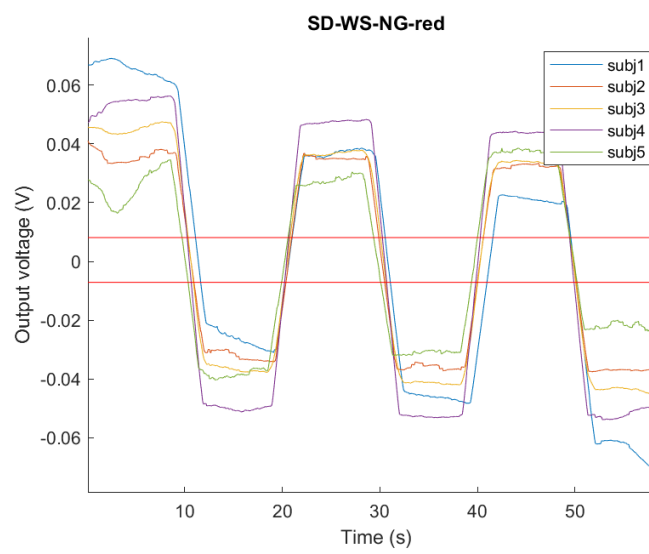


Figure 5.12: INA213 acquisition while subjects are sitting down, with shoes and without gloves, touching the drawers every 20 s for 10 s.

5.2 Power consumptions

A bench digital multimeter, AGILENT 34411A, has been used to measure both the transceiver and the receiver power consumptions. Table 5.2 shows transceiver power consumptions in terms of injected current during its regular operation, powering the INA333 or the INA213, and the receiver power consumptions during its regular operation and while it is performing the impedance mismatch (IM). Overall, it can be observed that power consumptions do not depend on DAC output and that they are consistently higher for RX, respect to the TX. Powering the INA333, this difference goes from 22 % (using the relè for both the TX and RX) until 47.8 % without using relè. Using the other instrumentation amplifier, power consumption increases because to power INA213, it is necessary to power the RX module, even if all the RX functions are not performed. Power consumption difference between measurements performed with the INA333 and the INA213 varies between the 13.2 %, obtained without powering relè, and the 20.3 % powering relè. Moreover, it has to be noted that powering the INA213 means powering the INA333 as well. This represents another reason why consumptions are so high. The last row shows the injected current range obtained while impedance mismatch is performed. It goes from almost the same value obtained in the second row to almost the same value of the first row, according to the fact that during performed tests, the relè is linking the front-end with the electrode for one second. When it is working, it absorbs around 15 mA, about 13.3 % of the RX's total power consumption.

Power consumption measurements during data exchange via Bluetooth have also been performed. During this type of test, the Bluetooth transmitter sent an array of characters: 'c i a o' every 50 ms, for 5 s. Then, other 5 s in which both devices did not send information and finally 5 s in which the previous Bluetooth receiver sent the same array to the previous transmitter. Table 5.3 and table 5.4 show results of this test, performed using both INA333 and INA213, with and without using TX and RX relè.

As it can be seen, there is a great difference between table 5.3 and the corresponding values of table 5.4, because of the use of both relè. It represents the same result obtained in table 5.2 and it is due to the significant amount of current required by relè.

	INA333		INA213	
	DAC=255	DAC=0	DAC=255	DAC=0
TX: injected current using the relè	92 mA	94 mA	106 mA	106 mA
TX: injected current without the relè	55 mA	55 mA	69 mA	69 mA
RX: Injected current using the relè	119 mA			
RX: injected current without the relè	105 mA			
RX: injected current while IM is performed	104 mA-120 mA			

Table 5.2: Power consumptions in terms of injected current for both TX and RX considering a square wave with an amplitude of 3.3 V and an amplitude equal to zero.

<i>Using relè</i>		Injected current		
		Transmission	Pause	Reception
TX	INA333	99 mA	94 mA	99 mA
	INA213	115 mA	109 mA	115 mA
RX		126 mA	155 mA	159 mA

Table 5.3: Power consumptions in terms of injected current for both TX and RX during data exchange via Bluetooth, powering both relè. Performed tests consist in 5 second in which the receiver sends data to the transceiver, then 5 seconds of pause and finally 5 seconds in which the transceiver sends data to the receiver.

Also during these measurements, INA213 was characterized by higher power consumptions, because in the meanwhile the RX module was powered as well as the unexploited INA333.

Moreover, it is essential to highlight that for the TX, for both the instrumentation amplifiers employed, the injected current during the transmission and reception period was the same, while for the RX, it was not. There is a higher value of

<i>Without relè</i>		Injected current		
		Transmission	Pause	Reception
TX	INA333	60 mA	54 mA	60 mA
	INA213	79 mA	74 mA	79 mA
RX		111 mA	140 mA	144 mA

Table 5.4: Power consumptions in terms of injected current for both TX and RX during data exchange via Bluetooth, without powering relè. Performed tests consist in 5 second in which the receiver sends data to the transceiver, then 5 seconds of pause and finally 5 seconds in which the transceiver sends data to the receiver.

injected current when the RX is receiving data via Bluetooth than when it is transmitting. This difference is equal to 33 mA in both tables (with and without relè), so it is significant also using the relè. The total amount of injected current for the RX, if it has to send data via Bluetooth, is 159 mA; too much, considering it is powered by batteries.

Chapter 6

Conclusions and Future Outcomes

This thesis aimed to maximize the touch detection module sensitivity and provide reliable support for visually impaired people for objects identification. A new board, which included both the transceiver and receiver module, was designed and plugged-in to two others, the Pyboard D-series with STM32F722 and WiFi/BT and the MicroPython pyboard D adapter with power management IC. The use of a new instrumentation amplifier, the INA213, has made it possible to achieve excellent results, considerably increasing the system sensitivity, compared to the previous version, which used the INA333. The resistance of the sensing resistor has been reduced by a factor of 10, avoiding the saturation of the amplifier. The system was tested on five subjects and three different size objects. Results confirmed the great sensitivity of the touch detection module. In fact, it can recognize the two signal levels even when the signal electrode is connected to a larger metal object which, acting as an antenna, significantly increases the noise. As regards touch recognition of the RX user, it was not possible to use mechanical switches at the RX level, preferring electronic ones, switching at higher frequencies and reducing the parasitic capacitance impedance. Results obtained are encouraging but not very repeatable and affected by noise.

Regarding future outcomes, reducing RX power consumptions has to represent one of the goals to pursue in order to support visually impaired people continuously. *Live Wire* can be further improved, making the RX user recognition and

the whole system more stable and more reliable, another step towards more secure communication. Finally, integrating TX and RX on the same board may be useful to place more *Live Wire* on the same object, i.e., the human body. Each module may act as TX or RX, switching its function and sending the local information collected to the other boards to allow safe and complete data exchange.

Bibliography

- [1] M. A. Callejon, D. Naranjo-Hernandez, J. Reina-Tosina, and L. M. Roa, “A comprehensive study into intrabody communication measurements,” *IEEE transactions on instrumentation and measurement*, vol. 62, no. 9, pp. 2446–2455, 2013.
- [2] M. Seyedi, B. Kibret, D. T. H. Lai, and M. Faulkner, “A survey on intrabody communications for body area network applications,” *IEEE transactions on biomedical engineering*, vol. 60, no. 8, pp. 2067–2079, 2013.
- [3] R. Cavallari, F. Martelli, R. Rosini, C. Buratti, and R. Verdone, “A survey on wireless body area networks: Technologies and design challenges,” *IEEE Communications surveys and tutorials*, vol. 16, no. 3, pp. 1635–1657, 2014.
- [4] M. Crepaldi, G. Zini, A. Maviglia, A. Barcellona, A. Merello, and L. Brayda, “Live wire: Body channel communication as a high impedance and frequency-scaled impulse radio,” in *2017 IEEE Biomedical Circuits and Systems Conference (BioCAS)*, 2017, pp. 1–4.
- [5] M. Crepaldi, A. Barcellona, G. Zini, A. Ansaldo, P. Motto Ros, A. Sanginario, C. Cuccu, D. De Marchi, and L. Brayda, “Live wire - a low-complexity body channel communication system for landmark identification,” *IEEE transactions on emerging topics in computing*, pp. 1–1, 2020.
- [6] B. Latré, B. Latré, B. Braem, B. Braem, I. Moerman, I. Moerman, C. Blondia, C. Blondia, P. Demeester, and P. Demeester, “A survey on wireless body area networks,” *Wireless networks*, vol. 17, no. 1, pp. 1–18, 2011.
- [7] Wikipedia, “Zigbee — wikipedia, l’enciclopedia libera,” 2020, [Online; in data 25-gennaio-2021]. [Online]. Available: <http://it.wikipedia.org/w/index.php?title=ZigBee&oldid=115420008>

- [8] Embedded security bodycom™ technology. [Online]. Available: <https://www.microchip.com/design-centers/embedded-security/technology/bodycom-trade-technology>
- [9] T. G. Zimmerman, “Personal area networks: Near-field intrabody communication,” *IBM Systems Journal*, vol. 35, no. 3.4, pp. 609–617, 1996.
- [10] M. Gray, “Physical limits of intra-body signalling,” Master thesis, Massachusetts Institute of Technology, 1997.
- [11] K. Partridge, B. Dahlquist, A. Veisoh, A. Cain, A. Foreman, J. Goldberg, and G. Borriello, “Empirical measurements of intrabody communication performance under varied physical configurations,” in *Proceedings of the 14th Annual ACM Symposium on User Interface Software and Technology*, ser. UIST '01. New York, NY, USA: Association for Computing Machinery, 2001, p. 183–190. [Online]. Available: <https://doi.org/10.1145/502348.502381>
- [12] M. Shinagawa, M. Fukumoto, K. Ochiai, and H. Kyuragi, “A near-field-sensing transceiver for intrabody communication based on the electrooptic effect,” *IEEE Transactions on Instrumentation and Measurement*, vol. 53, no. 6, pp. 1533–1538, 2004.
- [13] N. Cho, J. Yoo, S.-J. Song, J. Lee, S. Jeon, and H.-J. Yoo, “The human body characteristics as a signal transmission medium for intrabody communication,” *IEEE transactions on microwave theory and techniques*, vol. 55, no. 5, pp. 1080–1086, 2007.
- [14] S. Zhang, Y. Qin, J. Kuang, P. Mak, S. Pun, M. Vai, and Y. Liu, “Development and prospect of implantable intra-body communication technology,” *Journal of Computers*, vol. 9, 02 2014.
- [15] T. Handa, S. Shoji, S. Ike, S. Takeda, and T. Sekiguchi, “A very low-power consumption wireless ecg monitoring system using body as a signal transmission medium,” in *Proceedings of International Solid State Sensors and Actuators Conference (Transducers '97)*, vol. 2. IEEE, 1997, pp. 1003–1006 vol.2.
- [16] D. Lindsey, E. McKee, M. Hull, and S. Howell, “A new technique for transmission of signals from implantable transducers,” *IEEE transactions on biomedical engineering*, vol. 45, no. 5, pp. 614–619, 1998.
- [17] Y. K. a. a. K. Hachisuka, Y. Terauchi, “Simplified circuit modeling and fabrication of intra-body communication devices,” *Sensors and Actuators*, pp.

- 322–330, 2006.
- [18] M. Oberle, “Low power systems-on-chip for biomedical applications,” Ph.D. dissertation, ETH Zurich, Zürich, 2002, diss., Technische Wissenschaften ETH Zürich, Nr. 14509, 2002.
- [19] M. Wegmuller, “Intra-body communication (ibc) for biomedical sensor networks,” PhD Thesis, Switzerland: ETH, 2007.
- [20] Z. Tang, “Study on energy delivery rationale and method for implantable devices through volume conduction,” PhD Thesis, China: Chongqing University, 2007.
- [21] M. Sun, M. Mickle, W. Liang, Q. Liu, and R. Sciabassi, “Data communication between brain implants and computer,” *IEEE transactions on neural systems and rehabilitation engineering : a publication of the IEEE Engineering in Medicine and Biology Society*, vol. 11, pp. 189–92, 07 2003.
- [22] M. S. Wegmueller, S. Huclova, J. Froehlich, M. Oberle, N. Felber, N. Kuster, and W. Fichtner, “Galvanic coupling enabling wireless implant communications,” *IEEE Transactions on Instrumentation and Measurement*, vol. 58, pp. 2618–2625, 2009.
- [23] K. M. Al-Ashmouny, C. Boldt, J. E. Ferguson, A. G. Erdman, A. D. Redish, and E. Yoon, “Ibcom (intra-brain communication) microsystem: Wireless transmission of neural signals within the brain,” in *2009 Annual International Conference of the IEEE Engineering in Medicine and Biology Society*, 2009, pp. 2054–2057.
- [24] K. Foster and H. Schwan, “Dielectric properties of tissues and biological materials: a critical review.” *Critical reviews in biomedical engineering*, vol. 17 1, pp. 25–104, 1989.
- [25] S. Grimnes and Ørjan G Martinsen, “Chapter 3 - dielectrics,” in *Bioimpedance and Bioelectricity Basics (Third Edition)*, third edition ed., S. Grimnes and Ørjan G Martinsen, Eds. Oxford: Academic Press, 2015, pp. 37 – 75. [Online]. Available: <http://www.sciencedirect.com/science/article/pii/B9780124114708000039>
- [26] D. Miklavcic, N. Pavselj, and F. Hart, *Electric Properties of Tissues*, 04 2006, vol. 6.
- [27] O. Mårtensson, “Dielectric and electronic properties of biological materials. r. pethig. john wiley & sons, new york, 1979. 376 pp. price: \$15.00 (cloth),”

- International Journal of Quantum Chemistry*, vol. 17, no. 3, pp. 595–595, 1980. [Online]. Available: <https://onlinelibrary.wiley.com/doi/abs/10.1002/qua.560170316>
- [28] A. Marino, “Applied bioelectricity: From electrical stimulation to electropathology j. patrick reilly,” *The Quarterly Review of Biology*, vol. 74, p. 371, 09 1999.
- [29] K. Cole, “Permeability and impermeability of cell membranes for ions,” *Cold Spring Harbor Symposia on Quantitative Biology*, vol. 8, pp. 110–122, 1940.
- [30] J. Bae, H. Cho, K. Song, H. Lee, and H. Yoo, “The signal transmission mechanism on the surface of human body for body channel communication,” *IEEE Transactions on Microwave Theory and Techniques*, vol. 60, no. 3, pp. 582–593, 2012.
- [31] J. Wang, Y. Nishikawa, and T. Shibata, “Analysis of on-body transmission mechanism and characteristic based on an electromagnetic field approach,” *IEEE Transactions on Microwave Theory and Techniques*, vol. 57, no. 10, pp. 2464–2470, 2009.
- [32] F. Paone, “Touch-based user recognition system development and calibration protocol designing using a body channel communication prototype for visually impaired people indoor navigation,” 2020.
- [33] Pyboard d-series with stm32f722 and wifi/bt. [Online]. Available: <https://store.micropython.org/product/PYBD-SF2-W4F2>
- [34] Datasheet adg711/adg712/adg713. [Online]. Available: https://www.analog.com/media/en/technical-documentation/data-sheets/ADG711_712_713.pdf
- [35] Datasheet ina333. [Online]. Available: https://www.ti.com/lit/ds/symlink/ina333.pdf?ts=1612692759286&ref_url=https%253A%252F%252Fwww.google.com%252F
- [36] Datasheet ina210/ina211/ina212/ina213/ina214/ina215. [Online]. Available: https://www.ti.com/lit/ds/symlink/ina213.pdf?ts=1612695260299&ref_url=https%253A%252F%252Fwww.ti.com%252Fproduct%252FINA213%253FkeyMatch%253DINA213AIDCKR%2526tisearch%253DSearch-EN-Everything
- [37] Wbus-dip28 reference. [Online]. Available: https://pybd.io/hw/wbus_dip28.html

- [38] Datasheet ref1925/ref1930/ref1933/ref1941. [Online]. Available:
https://www.ti.com/lit/ds/symlink/ref1933.pdf?ts=1612879201715&ref_url=https%253A%252F%252Fwww.ti.com%252Fproduct%252FREF1933